NASA/TM—2001-210749/Chapter 5

Solid Lubrication Fundamentals and Applications

Abrasion: Plowing and Cutting

Kazuhisa Miyoshi
Glenn Research Center, Cleveland, Ohio

August 2001

The NASA STI Program Office . . . in Profile

Since its founding, NASA has been dedicated to the advancement of aeronautics and space science. The NASA Scientific and Technical Information (STI) Program Office plays a key part in helping NASA maintain this important role.

The NASA STI Program Office is operated by Langley Research Center, the Lead Center for NASA's scientific and technical information. The NASA STI Program Office provides access to the NASA STI Database, the largest collection of aeronautical and space science STI in the world. The Program Office is also NASA's institutional mechanism for disseminating the results of its research and development activities. These results are published by NASA in the NASA STI Report Series, which includes the following report types:

- TECHNICAL PUBLICATION. Reports of completed research or a major significant phase of research that present the results of NASA programs and include extensive data or theoretical analysis. Includes compilations of significant scientific and technical data and information deemed to be of continuing reference value. NASA's counterpart of peer-reviewed formal professional papers but has less stringent limitations on manuscript length and extent of graphic presentations.

- TECHNICAL MEMORANDUM. Scientific and technical findings that are preliminary or of specialized interest, e.g., quick release reports, working papers, and bibliographies that contain minimal annotation. Does not contain extensive analysis.

- CONTRACTOR REPORT. Scientific and technical findings by NASA-sponsored contractors and grantees.

- CONFERENCE PUBLICATION. Collected papers from scientific and technical conferences, symposia, seminars, or other meetings sponsored or cosponsored by NASA.

- SPECIAL PUBLICATION. Scientific, technical, or historical information from NASA programs, projects, and missions, often concerned with subjects having substantial public interest.

- TECHNICAL TRANSLATION. English-language translations of foreign scientific and technical material pertinent to NASA's mission.

Specialized services that complement the STI Program Office's diverse offerings include creating custom thesauri, building customized data bases, organizing and publishing research results . . . even providing videos.

For more information about the NASA STI Program Office, see the following:

- Access the NASA STI Program Home Page at ***http://www.sti.nasa.gov***

- E-mail your question via the Internet to help@sti.nasa.gov

- Fax your question to the NASA Access Help Desk at 301–621–0134

- Telephone the NASA Access Help Desk at 301–621–0390

- Write to:
  NASA Access Help Desk
  NASA Center for AeroSpace Information
  7121 Standard Drive
  Hanover, MD 21076

NASA/TM—2001-210749/Chapter 5

Solid Lubrication Fundamentals and Applications

Abrasion: Plowing and Cutting

Kazuhisa Miyoshi
Glenn Research Center, Cleveland, Ohio

National Aeronautics and
Space Administration

Glenn Research Center

August 2001

Available from

NASA Center for Aerospace Information
7121 Standard Drive
Hanover, MD 21076

National Technical Information Service
5285 Port Royal Road
Springfield, VA 22100

Available electronically at http://gltrs.grc.nasa.gov/GLTRS

Chapter 5
Abrasion: Plowing and Cutting

5.1 Introduction

Abrasion causes friction and wear by displacing material from one of two surfaces in relative motion. It may be caused by hard protuberances (asperities) on the second contact surface (two-body conditions) or by hard particles between the surfaces (three-body conditions) or embedded in one of them [5.1, 5.2]. The hard asperities and hard particles plow (groove) or cut one of the rubbing surfaces.

Abrasion is involved in the finishing of many surfaces. Filing, sanding, grinding, and lapping of engineering surfaces all involve abrasion. However, in many mechanical engineering systems abrasion is a common wear phenomenon of great economical importance. Approximately 50% of the wear encountered in industry is caused by abrasion mechanisms [5.3, 5.4].

A metal's resistance to abrasive wear is related to its static hardness under two-body conditions [5.5]. That is, the abrasive wear rate is inversely proportional to Vickers hardness for many annealed pure metals. Theory and experiments indicate that a metal's resistance to abrasive wear is proportional to the Vickers hardness of the fully work-hardened surface region [5.6]. Similar results have been obtained under three-body conditions [5.7].

Abrasion produces a worked or deformed layer and promotes a chemical interaction, as discussed in Chapter 2. For example, abrasion in a moist environment quickly admits hydrogen into aluminum, not only near the surface but in the bulk [5.8]. The solubility of hydrogen in aluminum is known to be low, only 0.6 atomic part per million (0.00006%) at the atmospheric pressure of hydrogen gas, even just below the melting point [5.9]. Aluminum is also highly reactive with water or oxygen and forms a chemically stable oxide surface, which is a strong chemical barrier against hydrogen permeation. Although these features of aluminum make the admission of hydrogen into aluminum difficult, the concentration of hydrogen admitted into aluminum by abrasion using an abrasive paper (silicon carbide (SiC) 800-mesh powder) is approximately two orders of magnitude greater than its solubility in aluminum at atmospheric pressure near the melting point. Hydrogen could lead to embrittlement and corrosion of materials.

5.2 Nature of Abrasion

Figures 5.1(a) and (b) are a scanning electron micrograph and an x-ray dispersive analysis map of a nearly spherical SiC particle and a groove, produced plastically by the plowing action of the particle, which slid and/or rolled on the softer metal surface [5.10]. Abrasion can arise when a hard particle or a hard asperity plows or cuts a series of grooves (Fig. 5.2, [5.11]). In plowing, the material first moves upward ahead of the particle's rake face and then moves around it into side ridges. In cutting, a ribbon of material is separated from the surface and moves upward past the rake face. How the material moves strongly depends on the nature of the surface; the tribological and bulk properties of the material, hard particle, or asperity; and the environment. Figures 5.3(a) and (b) are scanning electron micrographs of the wear tracks created on a manganese-zinc (Mn-Zn) ferrite ({100} surfaces) by sliding contact with a hemispherical (100-μm radius) diamond pin under dry and lubricated conditions. The lubricant was a high-purity olive oil, which is commonly used in fine lapping of ceramic materials and semiconductors. As shown, the tangential force introduced by sliding generated surface cracks much more easily in dry sliding than with the lubricant. The critical loads to fracture were 4 N in lubricated sliding and 1.5 N in dry sliding. Therefore, liquid lubrication of ceramics not only reduces friction and wear but also arrests crack formation.

Abrasion encountered in industrial situations can be broken down into two mechanisms: plowing and cutting. However, there are situations where one type changes to another or where the two mechanisms operate together.

5.3 Abrasion by Single Asperity

Experimental modeling and measurements can clarify the complex abrasion process and help in predicting friction and wear. The experiments can be conducted relatively simply by using a pin-on-flat sliding contact configuration. When a hard, spherical pin or wedge pin (e.g., Fig. 5.4) is brought into sliding contact with a softer flat surface, the materials behave both elastically and plastically. With rubber-like materials the elastic properties play an important role in contact deformation. With ductile and semiductile materials, such as metals and intermetallic compounds, however, the behavior is different. Although the elastic moduli are large, the range over which metals deform elastically is relatively small. Consequently, when metals are deformed or indented, the deformation is predominantly outside the elastic range. Often, a plastically deformed groove (Fig. 5.5) is generated in plowing, or a ribbon-like metal chip (Fig. 5.6) moves upward past the wedge's rake face in cutting. The sliding involves plastic flow and generates a considerable amount of metal wear debris.

Brittle materials, such as ceramics and some intermetallic compounds, behave micromechanically in a ductile fashion up to a certain contact stress when in contact with themselves or other solids. Even at room temperature ceramics, such as

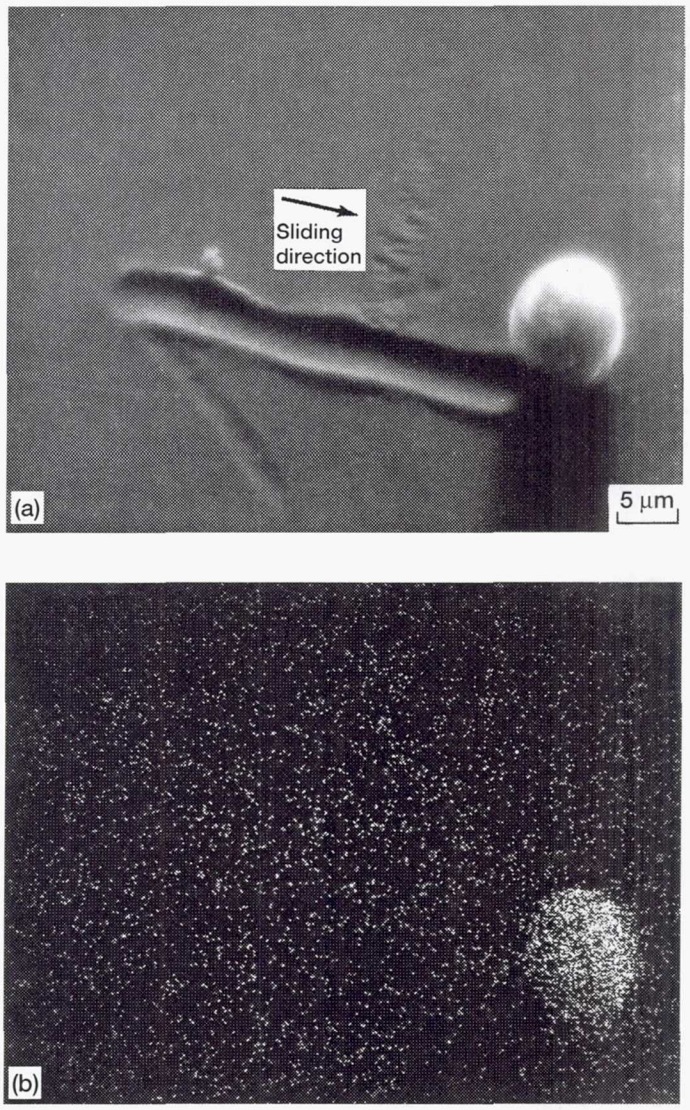

Figure 5.1.—Scanning electron micrograph and x-ray dispersive analysis of wear scar produced by spherical SiC particle on alloy in vacuum (10^{-8} Pa). Sliding velocity, 3 mm/min; load, 0.2 N; room temperature. (a) Spherical SiC particle and groove. (b) Silicon K_α x-ray map on 1.02 at.% Ti-Fe alloy.

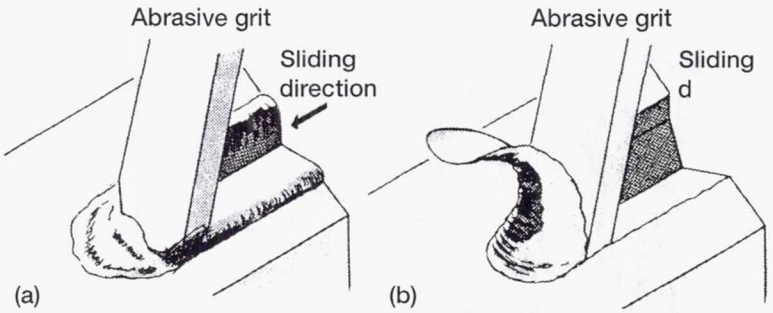

Figure 5.2.—Abrasion models. (a) Plowing. (b) Cutting.

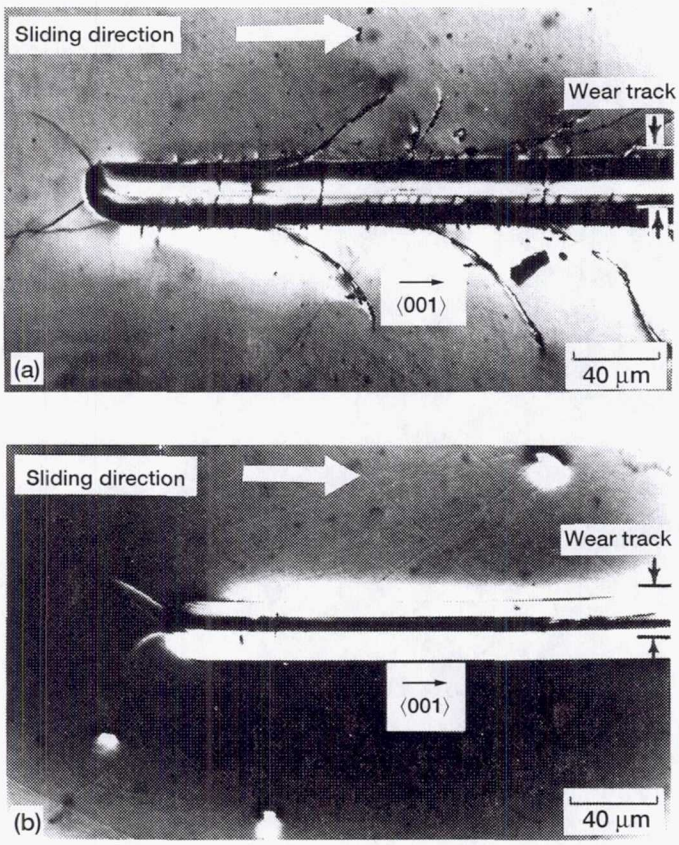

Figure 5.3.—Diamond pin sliding on single-crystal Mn-Zn ferrite {100} surface. (a) In air. (b) Lubricated with olive oil.

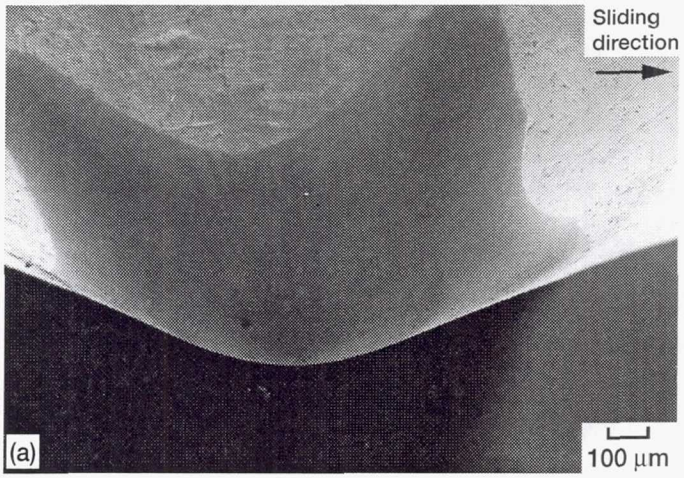

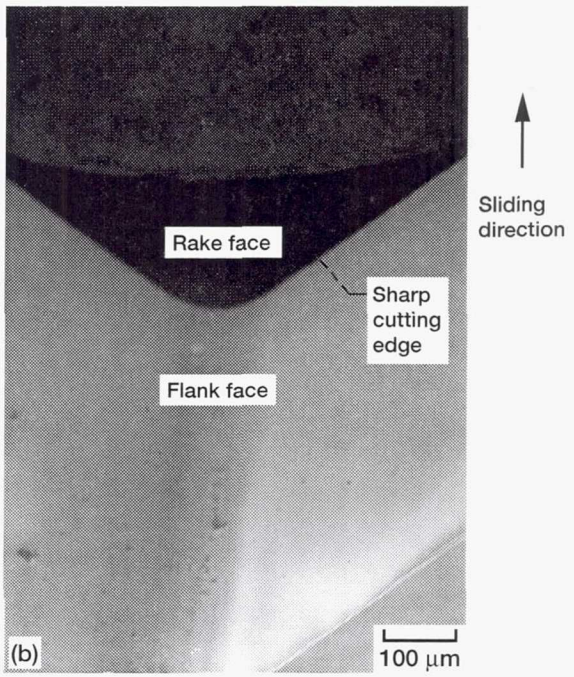

Figure 5.4.—Idealized diamond abrasive particles. (a) Single-crystal spherical pin (0.2-mm radius). (b) Single-crystal wedge (sliding direction perpendicular to rake face).

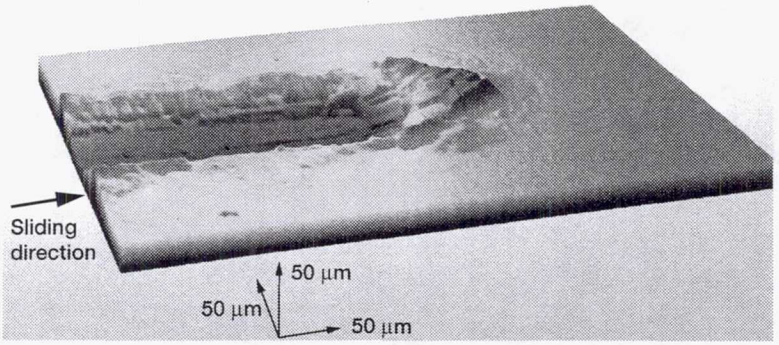

Figure 5.5.—Plastically deformed groove on γ-TiAl surface produced by single-pass sliding of 0.2-mm-radius diamond pin at 30-N load.

aluminum oxide (Al_2O_3) and SiC, behave both elastically and plastically at low stresses under relatively modest rubbing contact, but they microfracture under more highly concentrated contact stresses [5.12–5.19]. This microfracture, known as brittle fracture, is detrimental to the reliability of ceramics and must be considered in designing for structural and tribological applications.

Thus, the deformation and fracture behavior of materials, which plays an important role in assessing abrasive friction and wear, falls into three main categories: elastic contact, plastic contact, and brittle contact.

5.3.1 Plowing by Spherical Pin

In elastic contact (Fig. 5.7(a)) the coefficient of friction decreases as the load increases. The relation between coefficient of friction μ and load W is given by [5.20]:

$$\mu = KW^{-1/3} \tag{5.1}$$

The minus 1/3 power can be interpreted simply as arising from an adhesion mechanism, with the contact area being determined by elastic deformation. In elastic contact frictional energy is dissipated during sliding by shearing at the interface. By contrast, in plastic contact the coefficient of friction increases as the load increases (Fig. 5.7(b)), a complete reversal in friction behavior from that in elastic contact. In plastic contact frictional energy is dissipated during sliding by shearing at the interface and by plastic deformation of the soft material (i.e., plowing of the soft flat by the hard pin).

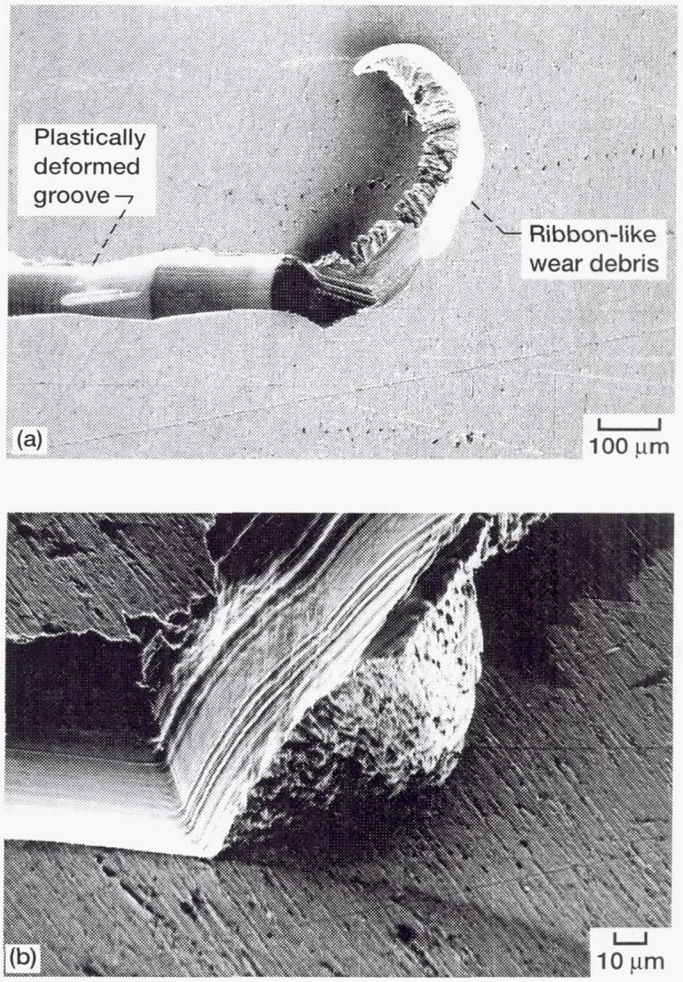

Figure 5.6.—Ribbon-like wear debris and plastically deformed groove on aluminum surface produced by single-pass sliding of diamond wedge. (a) Overview of groove and ribbon. (b) High magnification.

With a brittle solid, such as a ceramic, under high contact pressure, sliding action causes gross surface and subsurface cracking as well as plastic deformation [5.17]. Cracking produces wear debris particles and large fracture pits. The area of a fracture pit is a few times larger than the area of the plastically deformed groove. The coefficient of friction is also much higher in brittle contact (Fig. 5.7(c)) than in elastic and plastic contacts. In brittle contact frictional energy is dissipated during sliding by shearing at the interface, by plastic deformation of the soft material, and by cracking in the brittle material [5.21, 5.22].

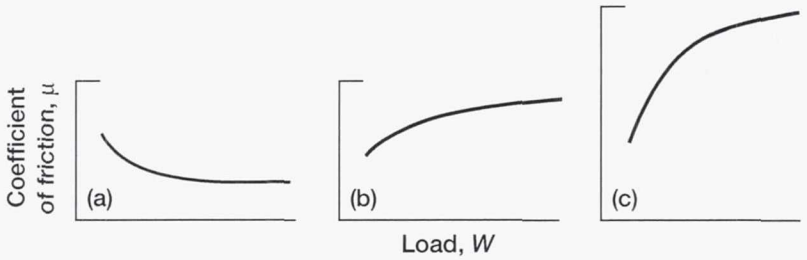

Figure 5.7.—Schematic representation of load effect on coefficient of friction for spherical, hard pin sliding on flat, soft solid. (a) Elastic contact. (b) Plastic contact. (c) Brittle contact.

Elastic contact.—Figure 5.8(a) presents coefficients of friction measured for a smooth polyester film (23 μm thick and 12.7 mm wide) in sliding contact with a smooth, polycrystalline nickel-zinc (Ni-Zn) ferrite, spherical pin (2-mm radius) in humid air at various loads. The data clearly indicate that the coefficient of friction decreased as the load increased. With sliding, elastic deformation occurred in the surfaces of both the polyester film and the polycrystalline Ni-Zn ferrite pin [5.23].

Another example of friction behavior in elastic contact is shown in Fig. 5.8(b). When boron nitride (BN) deposited on an AISI 440C stainless steel flat was placed in sliding contact with BN deposited on a 440C stainless steel, hemispherical pin at various loads in ultrahigh vacuum, the coefficient of friction decreased as the load increased. To a first approximation for the load range investigated, the relation between coefficient of friction μ and load W on logarithmic coordinates is given by $\mu = 0.29W^{-1/3}$ for sputter-cleaned specimen couples and $\mu = 0.17W^{-1/3}$ for as-received specimen couples. The friction was a function of the shear strength of this elastic contact area [5.18]. Thus, ceramics behave elastically up to a certain load under sliding contact.

Transition from elastic to plastic contact.—Single-pass and multipass sliding friction experiments were also conducted with the three tapes in Table 5.1 in contact with a polycrystalline Ni-Zn ferrite, spherical pin (2-mm radius) in laboratory air at various loads. Friction traces were relatively smooth, with no evidence of stick-slip. As the load increased, the coefficient of friction decreased, up to 0.25 N, and then increased (Fig. 5.9). When repeated passes were made, the coefficient of friction generally exhibited only small changes with the number of passes at any load up to 1.0 N (data not shown). The data of Fig. 5.9 raise the question of how the interface deforms with sliding action.

The wear tracks on the tape, which the ferrite pin was made to traverse, varied with different loads up to 1.0 N when examined by optical and scanning electron microscopes. At 0.1 N essentially no detectable wear track existed on the tape surface, which looked like the surface of the as-received magnetic tape (as shown in Chapter 4, Fig. 4.21(a)). At loads up to 0.25 N, although sliding occurred at the interface, both the tape and the Ni-Zn ferrite pin deformed elastically. At 0.25 N and

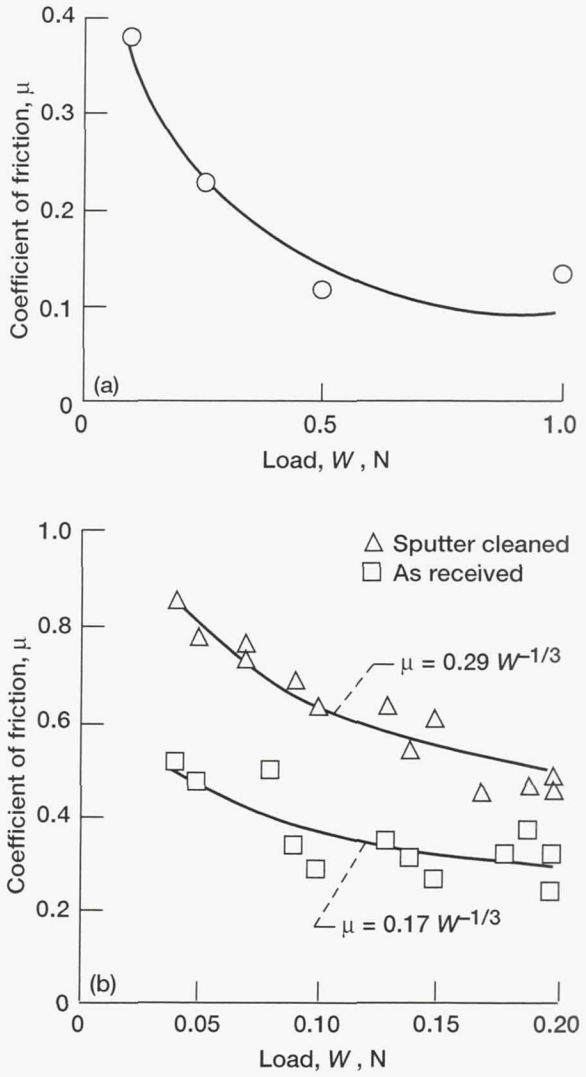

Figure 5.8.—Coefficient of friction as function of load in elastic contact. (a) Ni-Zn ferrite pin (2-mm radius) sliding on polyester film. Sliding velocity, 1.5 mm/min; relative humidity, 40%; temperature, 23 °C. (b) BN film deposited on hemispherical pin in contact with BN film deposited on flat in vacuum.

TABLE 5.1.—COMPOSITION AND PROPERTIES OF MAGNETIC TAPES
[Polyester base film 23 μm thick and 12.7 mm wide. From [5.23].]

Tape	Magnetic particle	Binder	Lubricant	Surface roughness,[a] nm	Knoop hardness at 23 °C,[b] MPa
1	CrO_2	Polyester-polyurethane and phenoxy	Butyl stearate and butyl palmitate	14.4	225
2	γ-Fe_2O_3	Polyester-polyurethane and epoxy	Butyl myristate	8.5	157
3	Cobalt-doped γ-Fe_2O_3	Polyester-polyurethane, polyvinyl chloride, and polyvinyl acetate	Butyl ethyl stearate	13.6	118

[a]Root-mean-square roughness.
[b]Measuring load of hardness, 0.0013 N.

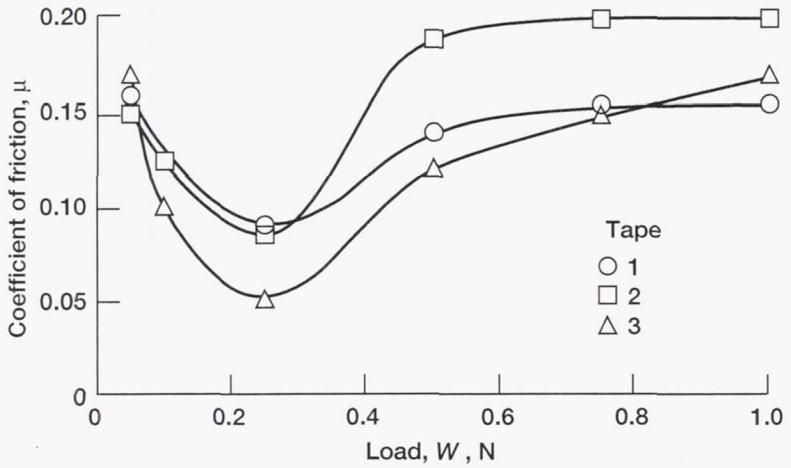

Figure 5.9.—Coefficient of friction as function of load for Ni-Zn ferrite pin (2-mm radius) sliding on magnetic tapes (tapes 1 to 3 in Table 5.1). Sliding velocity, 1.5 mm/min; relative humidity, 40%; temperature, 23 °C.

above the Ni-Zn ferrite pin primarily deformed elastically, but the tape deformed plastically. The sliding action produced a visible wear track on the magnetic tape. Figure 4.21(b) shows the blunt appearance, resulting primarily from plastic deformation, of the asperities on the wear track after five sliding passes at 1.0 N.

Plastic contact.—When a monolithic SiC surface was placed in sliding contact with a spherical diamond pin under relatively low load (up to 0.5 N), elastic deformation occurred in both surfaces (Fig. 5.10(a)). With the initiation of tangential motion, sliding occurred at the interface. Under these low loads neither groove formation due to plastic flow nor SiC cracking during sliding was observed. Friction was a function of the shear strength of the elastic contact area (i.e., the relation

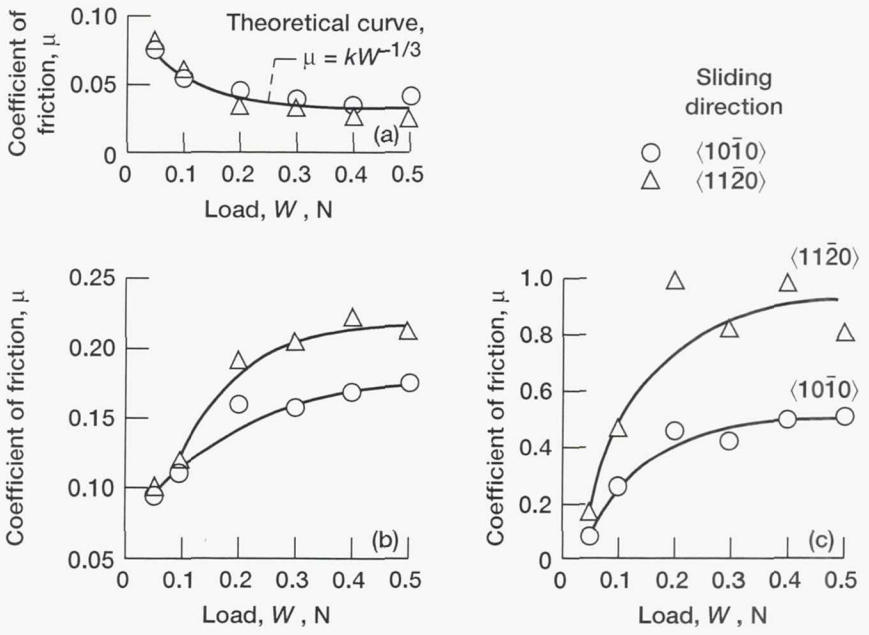

Figure 5.10.—Coefficient of friction as function of load for hemispherical diamond pins of different radii and conical diamond pin sliding on {0001} surface of single-crystal SiC in argon at atmospheric pressure. (a) Elastic contact (diamond radius, 0.3 mm). (b) Plastic contact (diamond radius, 0.02 mm). (c) Brittle contact (conical diamond pin with apical angle of 117°).

between coefficient of friction μ and load W is given by Eq. (5.1)). Over the entire load range the mean contact pressure ranged from 1.5 to 3.5 GPa. The maximum pressure at the center of the contact area calculated from a Hertzian stress distribution was 2.3 to 4.9 GPa.

Silicon carbide, like most ceramics, both in monolithic and in coating form, deforms in a ductile fashion as the contact pressure is increased. The increase in applied load, however, results in a complete reversal in friction characteristic from that in elastic contact. Figure 5.10(b) reveals an entirely different mode of deformation and energy dissipation with an estimated maximum Hertzian contact pressure ranging from 14 to 30 GPa. Plastic deformation occurred in the SiC, causing permanent grooves during sliding, but there was little or no evidence of small cracks being generated in the SiC. The diamond pin indented the SiC without suffering any permanent deformation itself. The frictional energy dissipated during sliding following solid-state contact was caused by shearing at the interface and by plastic deformation of the SiC (i.e., plowing by the diamond). The relation between coefficient of friction μ and load W now took the form

$$\mu = kW^m \tag{5.2}$$

where $m = 0.3$ to 0.4. The exponent m depends on the crystallographic orientation, plastic deformation, and hardness of the single-crystal SiC.

With a conical diamond pin (117° apical angle with radius of curvature at apex less than 5 μm), ceramics behave in a brittle fashion (Fig. 5.10(c)). This subject is discussed in the next section.

Similar contact and friction characteristics also occurred for diamond pins (0.2-mm radius) on BN films [5.18, 5.19]. At certain loads the sliding action of the diamond pin permanently grooved the BN films deposited on both metallic [5.18] and nonmetallic [5.19] substrates. For example, Fig. 5.11 presents the widths of plastically deformed grooves in BN films on 440C stainless steel substrates. Comparative data for uncoated 440C stainless steel are also presented. When the widths D of the resulting grooves in the BN films are plotted against the load W on logarithmic coordinates, the data can be expressed as Meyer's law:

$$W = kD^n \tag{5.3}$$

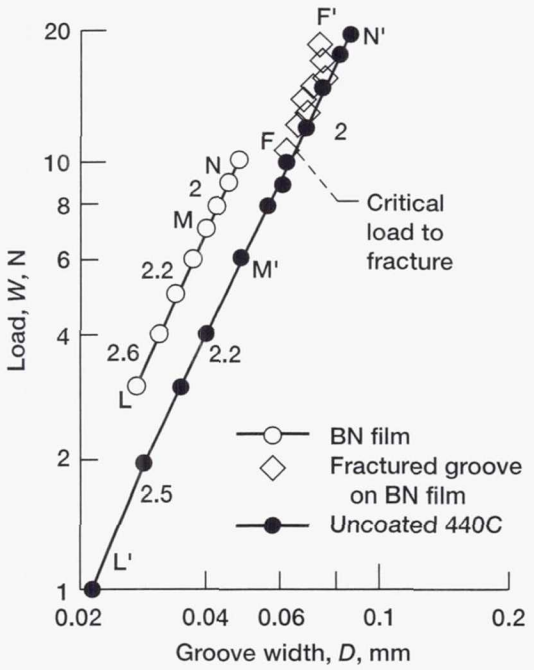

Figure 5.11.—Groove width as function of load for BN film deposited on 440C stainless steel in contact with hemispherical diamond pin (2-mm radius) in laboratory air.

The portions of the curves LM for the BN film and L′M′ for the uncoated 440C stainless steel are considered to be approximately straight with transitional slopes of 2.6, 2.5, and 2.2. The portions MN for the BN film and M′N′ for the uncoated 440C stainless steel are straight lines with a slope of 2. The portions MN and M′N′ are the ranges over which Meyer's law is valid for BN film and for uncoated 440C stainless steel. Here the Meyer index n is constant and equal to 2. Thus, BN films on metallic [5.18] and nonmetallic [5.19] substrates behave plastically much like metals when they are brought into contact with hard solids such as diamond [5.18, 5.24]. The contact pressure gradually increases until deformation passes to a fully plastic state. The mean contact pressure P_m at a fully plastic state increases by a factor of 2 with the presence of BN film. When the load exceeds a certain critical value, the sliding action of diamond on the monolithic SiC and on the BN film causes fracture in both specimens.

The width D and height H of a groove are defined in Fig. 5.12. The mean contact pressure P_m during sliding may be defined by $P_m = W/A_s$, where W is the applied load and A_s is the projected contact area given as $A_s = \pi D^2/8$. Only the front half of the pin is in contact with the flat. The relation between the groove width generated by the pin and the load is expressed by $W = kD^n$, which is known as Meyer's law [5.25].

Brittle contact.—With a conical diamond pin (causing highly concentrated stress in the contact area between diamond and SiC), sliding action produces gross surface and subsurface cracking as well as plastic deformation [5.17]. Under such conditions wear debris particles and large fracture pits caused by cracking are observed. The SEM observation indicated that the area of a fracture pit is a few times larger than the area of the plastically deformed groove. The coefficient of friction in brittle contact (Fig. 5.10(c)) is also much higher (four times or more) than in elastic and plastic contacts. Although fracture and plastic deformation in SiC are responsible for the friction behavior observed, most of the frictional energy dissipation during sliding is caused by the fracturing of the SiC. Therefore, the coefficient of friction

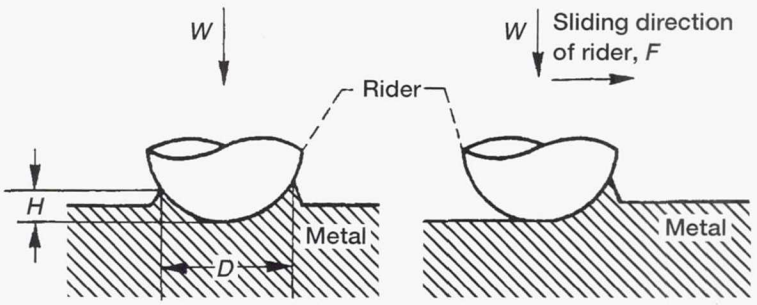

Figure 5.12.—Deformation of metal. (a) End view (lateral cross section). (b) Side view (longitudinal cross section).

is commonly influenced by the bulk properties of the ceramic, such as fracture toughness and crystallographic orientation (Fig. 5.10(c), [5.17]).

For BN films deposited onto metallic or nonmetallic substrates [5.18, 5.19], failure occurs primarily in the film or at the interface between film and substrate (or both) when the film is critically loaded. For example, in Fig. 5.11 the portion FF′, representing the condition of fracture where the load exceeds the critical load, is also roughly expressed by $W = kD^n$. The fractured groove in the BN film is almost as wide as the groove in the uncoated 440C. The evidence confirms that cracks are generated from the contact area rather than from the free surface of the film. It suggests that the substrate is responsible not only for controlling the critical load, which will fracture the BN film, but also for the extent of fracture. Furthermore, the critical load required to fracture a ceramic film on a substrate can be determined by measuring the groove width.

Effects of shear strength of metals.—Abrasion both causes plastic deformation and generates metal wear debris. The metal removal mechanisms are plastic deformation, surface fatigue, and adhesive wear. Although experimental modeling by using spherical pins indeed represents some typical abrasive wear phenomena, it does not represent the principal mechanisms of metal removal in abrasion. The shear strength of the metal must also be taken into account. Abrasion occurs, for example, when SiC grit slides on metals and alloys, causing plastic flow and generating metal wear debris. A spherical SiC pin sliding on iron (Fig. 5.13) resulted in a permanent groove in the iron surface, with a considerable amount of deformed metal piled up along the groove sides, and metal wear debris. The wear debris particles were primarily on the sides of the wear track or transferred to the SiC pin at its tip. Much less metal debris was removed, however, than the volume of the groove plowed out by the SiC pin.

When relatively ductile metals, such as magnesium, aluminum, copper, zirconium, and iron (Table 5.2, [5.11]), are worn in abrasion, the principal mechanism of metal removal is chip formation in front of the cutting abrasive, which often is angular in shape [5.26–5.28]. The few exceptions to this mechanism include abrasion by abrasives that are soft relative to the metal and abrasion by lightly loaded, round abrasives. In these cases metal is removed at a relatively low rate (discussion by Jorn Larsen-Basse in [5.11]). For example, abrasion on dry emery leads to an amount of wear (metal removal) corresponding to only about 10% of the volume of the grooves plowed out by the abrasives [5.27].

A spherical pin will remove chips from a metal surface when the ratio between the groove height and the sphere radius $H/R > 0.1$. For $H/R < 0.01$ only elastic deformation takes place, and for $0.01 < H/R < 0.1$ material flows by plastic deformation to ridges along the groove sides [5.29]. For example, when $R = 25$ μm, the two values of H are 2.5 μm and 0.25 μm, respectively.

In consideration of $0.01 < H/R < 0.1$ and to obtain geometrically similar grooves, experiments with the relatively ductile metals shown in Table 5.2 were conducted at a load of 0.049 N; and experiments with relatively harder metals, such as titanium,

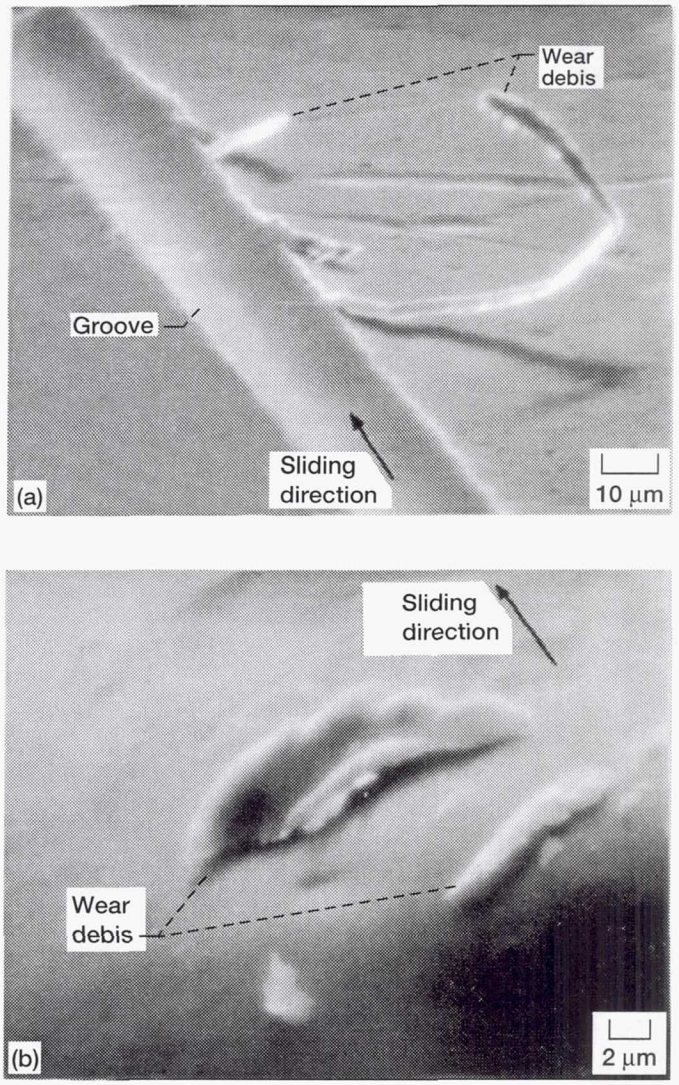

Figure 5.13.—Iron wear debris and groove. Single-pass sliding of 0.04-mm-radius SiC pin; sliding velocity, 3 mm/min; load, 0.25 N; temperature, 25 °C; environment, argon; pressure, atmospheric. (a) Iron wear debris and groove on iron surface. (b) Iron wear debris transferred to SiC.

TABLE 5.2.—CRYSTALLINE, PHYSICAL, AND CHEMICAL PROPERTIES OF METALS

Metal	Purity,[a] percent	Crystal structure at 25 °C[b]	Lattice constant,[c] Å (10^{-10} m)	Cohesive energy[b]		Shear modulus,[b] Pa
				J/g·atom	kcal/g·atom	
Iron	99.99	(c)	a = 2.8610	416.0×10^3	99.4	8.15×10^{10}
Chromium			a = 2.8786	395	94.5	11.7
Molybdenum			a = 3.1403	657.3	157.1	11.6
Tungsten			a = 3.1586	835.5	199.7	15.3
Aluminum		(d)	a = 4.0414	322	76.9	2.66
Copper	99.999		a = 3.6080	338	80.8	4.51
Nickel	99.99		a = 3.5169	428.0	102.3	7.50
Rhodium			a = 3.7956	556.5	133.0	14.7
Magnesium		(e)	a = 3.2022; c = 5.1991	148	35.3	1.74
Zirconium			a = 3.223; c = 5.123	609.6	145.7	3.41
Cobalt			a = 2.507; c = 4.072	425.5	101.7	7.64
Titanium	99.97		a = 2.923; c = 4.729	469.4	112.2	3.93
Rhenium	99.99		a = 2.7553; c = 4.4493	779.1	186.2	17.9

[a]Manufacturer's analysis.
[b]From [5.40].
[c]Body-centered cubic
[d]Face-centered cubic.
[e]Hexagonal close packed.
[f]From [5.41].

nickel, rhodium, molybdenum, and tungsten (Table 5.2), were conducted at a load of 0.2 N. Mineral oil was used to minimize adhesion. When a spherical, 25-μm-radius SiC pin was put in sliding contact with the various metal disks, the coefficient of friction and the groove height linearly decreased and the contact pressure linearly increased as the shear strength of the metal increased (Fig. 5.14), for both the ductile and harder metals without exception. The coefficient of friction, particularly its plowing term, and the groove height corresponding to the groove volume may be governed by two factors: the shear strength at the interface and the shear strength of the bulk metal. Thus, the data presented in Fig. 5.14 fall within the range $0.01 < H/R < 0.1$, where only elastic and plastic surface deformation are expected.

Alloying element effects.—There is no doubt that a solid's structure plays an important role in its tribological behavior, such as adhesion and friction behavior, as discussed in Chapter 3. For example, solid-solution alloying, a major mode of metal strengthening, influences friction and deformation behavior under abrasive conditions. Figures 5.15 and 5.16 present the coefficients of friction and the groove heights (corresponding to the groove volume) as a function of solute concentration (in atomic percent) for a number of binary alloys in sliding contact with 25-μm-radius, spherical, single-crystal SiC pins at loads of 0.05 and 0.1 N in mineral oil. The iron-base binary alloy systems were alloyed with manganese, nickel, chromium, rhodium, tungsten, or titanium. The coefficient of friction and the groove height decreased as the solute concentration increased. The coefficient of friction

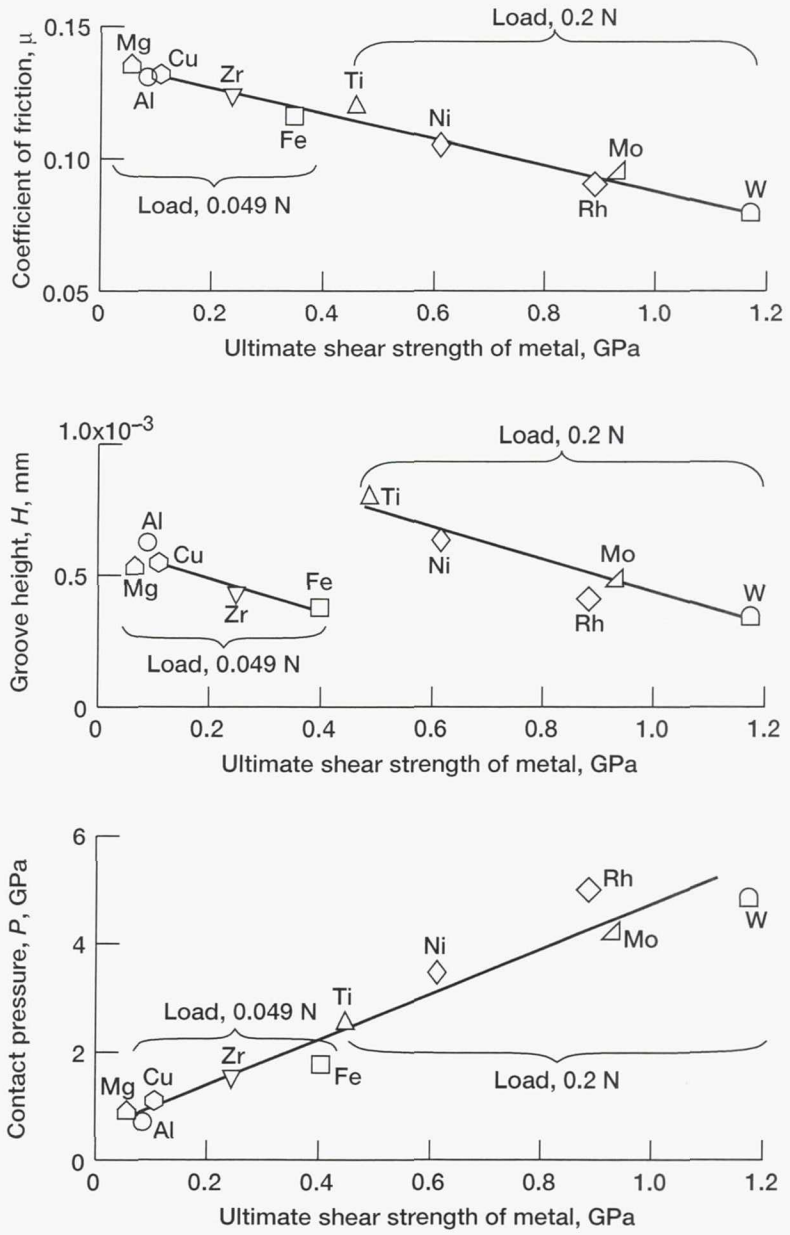

Figure 5.14.—Coefficient of friction, groove height, and contact pressure as function of shear strength for various metals. Single-pass sliding of 25-μm-radius SiC pin in mineral oil; sliding velocity, 3 mm/min; load, 0.049 or 0.2 N; temperature, 25 °C.

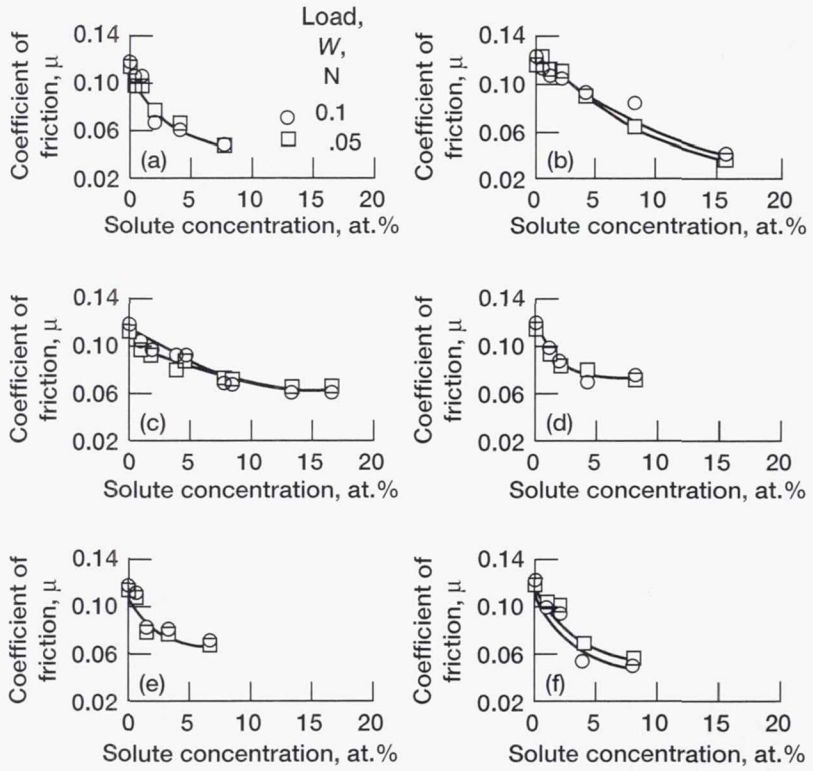

Figure 5.15.—Coefficient of friction as function of solute concentration for various iron-base alloys and pure iron. Single-pass sliding of 25-μm-radius SiC pin in mineral oil; sliding velocity, 3 mm/min; temperature, 25 °C. (a) Iron-manganese alloy.(b) Iron-nickel alloy. (c) Iron-chromium alloy. (d) Iron-rhodium alloy. (e) Iron-tungsten alloy. (f) Iron-titanium alloy.

did not change significantly with load (Fig. 5.15), but there were obvious differences in the groove height with load (Fig. 5.16). The average rates of decrease in the coefficient of friction and the groove height strongly depended on the alloying element.

Figure 5.17 presents the contact pressures (groove microhardnesses) during sliding under the same conditions as in Figs. 5.15 and 5.16 for the same binary alloys as a function of solute concentration (in atomic percent). The contact pressure was calculated from the groove width. It increased as the solute concentration increased, with the average rates of increase depending on the alloying element. The contact pressure did not change significantly with load. Controlling mechanisms for the friction and deformation of iron-base binary alloys are discussed next.

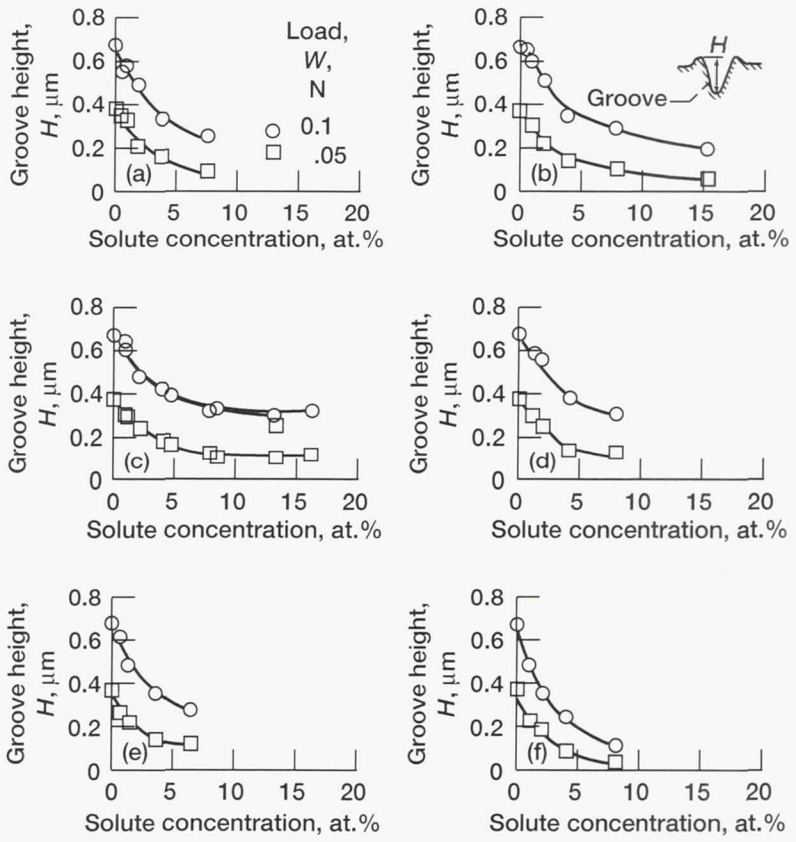

Figure 5.16.—Groove height as function of solute concentration for various iron-base alloys and pure iron. Same conditions as for Fig. 5.15. (a) Iron-manganese alloy. (b) Iron-nickel alloy. (c) Iron-chromium alloy. (d) Iron-rhodium alloy. (e) Iron-tungsten alloy. (f) Iron-titanium alloy.

The grooves (wear tracks) in this investigation were formed in the alloys primarily by plastic deformation under hydrostatic contact pressure and the plowing stress associated with sliding. In addition, there was occasional material removal (wear debris fragments) [5.11]. The formation of grooves may be similar to the formation of hardness test indentations. Therefore, the manner in which the friction and wear properties correlate with the solute-to-iron atomic radius ratio or atomic size misfit is of interest. Alloy hardening at high temperatures (300 and 411 K) and alloy softening at lower temperatures (77 and 188 K) have been observed in several iron-base binary alloys [5.30–5.34]. These investigations concluded that for many alloy systems both alloy softening and alloy hardening were controlled by atomic

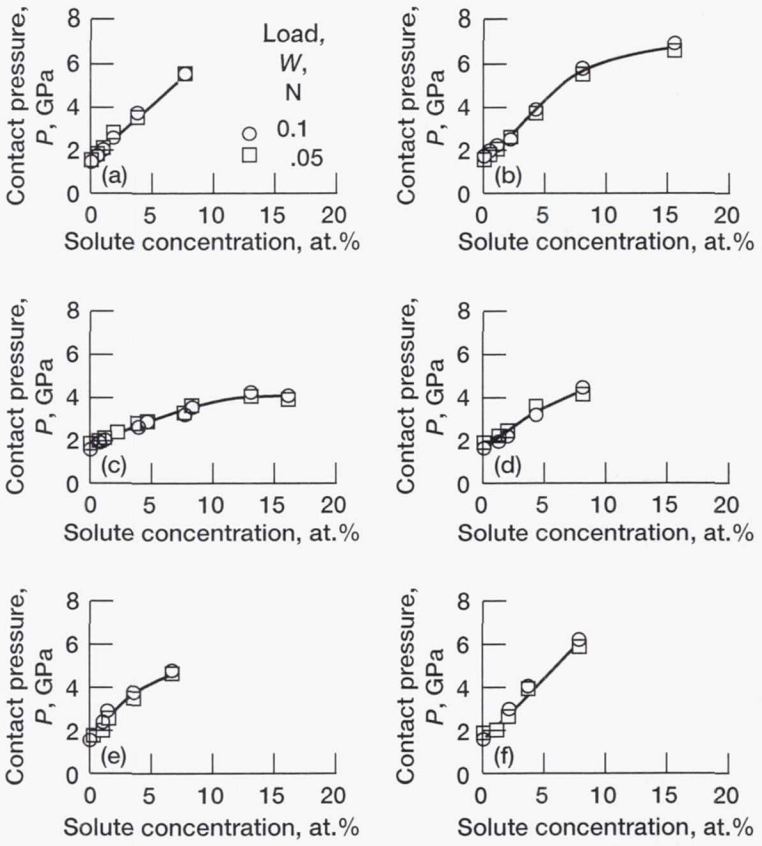

Figure 5.17.—Contact pressure (calculated) as function of solute concentration for various iron-base alloys and pure iron. Same conditions as for Fig. 5.15. (a) Iron-manganese alloy. (b) Iron-nickel alloy. (c) Iron-chromium alloy. (d) Iron-rhodium alloy. (e) Iron-tungsten alloy. (f) Iron-titanium alloy.

size misfit or solute-to-iron atomic radius ratio. The atomic size misfit parameter was concluded to be a reasonably good indicator that α-iron was strengthened by adding a low concentration of substitutional solutes [5.30].

Figure 5.18 presents the decreasing rates of coefficient of friction $-d\mu/dC$ and groove height $-dH/dC$ and the increasing rate of contact pressure dP/dC with increasing solute concentration C as a function of solute-to-iron atomic radius ratio K at loads of 0.1 and 0.05 N. The rates were estimated from the data in Figs. 5.15 to 5.17. That is, the rate is the difference between the maxima and minima of coefficient of friction, groove height, or contact pressure divided by the maximum

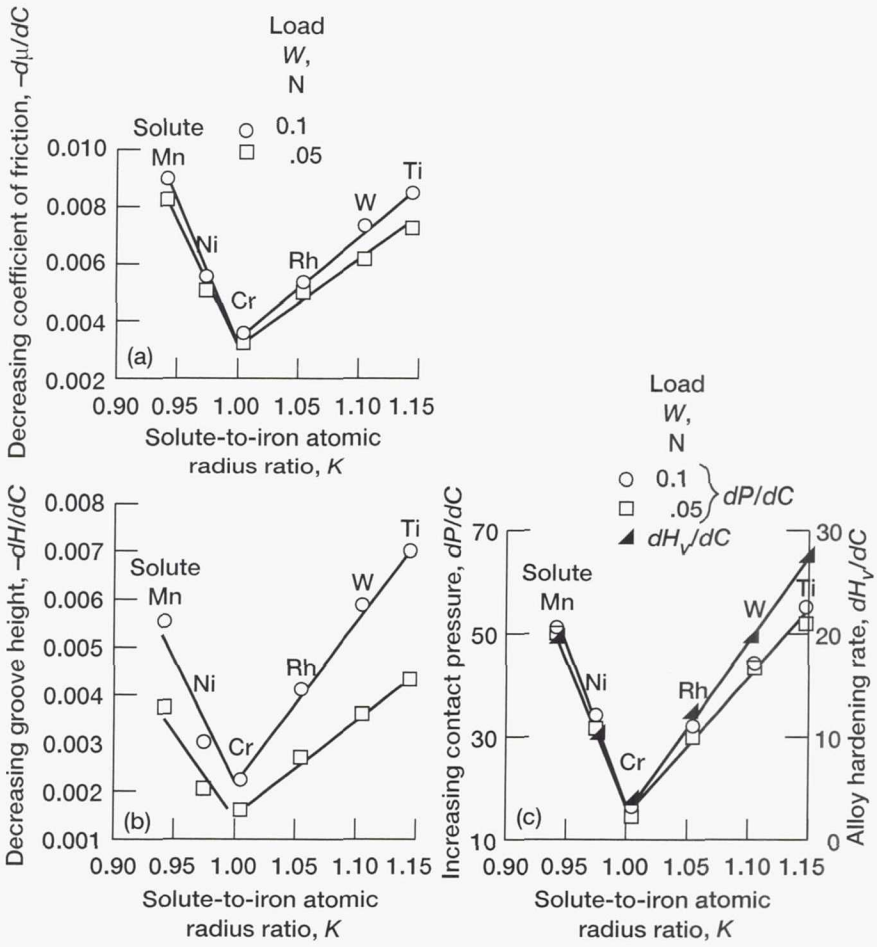

Figure 5.18.—Rates of change of coefficient of friction, groove height, and contact pressure as function of solute-to-iron atomic radius ratio.

solute concentration in each alloy. Agreement is good between the friction and deformation (wear) properties and the solute-to-iron atomic radius ratio. The correlation for each rate is separated into two cases: first, the case for alloying with manganese and nickel, which have smaller atomic radii than iron; and second, the case for chromium, rhodium, tungsten, and titanium, which have larger atomic radii than iron. The $-d\mu/dC$, $-dH/dC$, and dP/dC increase as the solute-to-iron atomic radius ratio increases or decreases from unity. The rates of change are a minimum at unity. Thus, the correlations indicate that the atomic size of the solute, as well as

alloy hardening (Fig. 5.18(c), [5.34]), is an important parameter in controlling abrasive wear and friction in iron-base, binary alloys.

Deformation effects of mechanical polishing.—The effect of mechanical polishing on abrasive wear was examined. Spherical, 25-μm-radius SiC pins were slid on mechanically polished, iron-titanium binary alloy disk surfaces in both the annealed and unannealed (polished) states in mineral oil at loads of 0.05, 0.1, and 0.2 N [5.35]. The coefficient of friction and the groove height generally decreased and the contact pressure (corresponding to the microhardness) increased as the titanium concentration increased (Fig. 5.19). These changes were larger for the annealed surfaces than for the unannealed surfaces, but the trends for both surfaces were similar.

Crystallographic orientation (anisotropy) effects.—Metals and ceramics exhibit anisotropic behavior in many of their mechanical, physical, and chemical properties. Under abrasion conditions (just as under adhesive conditions described in Chapter 3), the differences in the coefficients of friction with respect to the crystallographic plane and direction are also significant, as discussed for single-crystal SiC in Section 2.2.1 (Fig. 2.10). The friction, deformation, fracture, and wear behaviors of single-crystal ceramics are anisotropic. Both oxide and nonoxide ceramics exhibit anisotropic abrasion and friction behavior.

Figure 5.20 presents the coefficient of friction as a function of the crystallographic sliding direction on the {100}, {110}, {111}, and {211} planes of Mn-Zn ferrite in sliding contact with a 20-μm-radius, spherical diamond pin at a 1-N load in laboratory air. As a reference, the Knoop hardness is also presented as a function of the crystallographic direction on the four planes of Mn-Zn ferrite. The sliding caused primarily plastic flow as well as surface cracking in the ferrite. The coefficient of friction was influenced by the crystallographic orientation. The anisotropic friction and plastic deformation of Mn-Zn ferrite may be controlled by the slip systems $\{110\}\langle 110\rangle$. In general, the softer the crystallographic direction, the greater the coefficient of friction.

5.3.2 Cutting by Wedge Pin

When a diamond wedge pin (Fig. 5.4(b)) slid on a metal flat surface lubricated with a drop of perfluoropolyether oil at a load of 0.2 N, the coefficient of friction, the volume of metal displaced in unit load and unit distance (wear rate), and the metal's wear resistance (the inverse of wear rate) correlated with the Vickers hardness of the metal (Fig. 5.21). Perfluoropolyether oil was used to minimize adhesion. The wedge's longitudinal, 50-μm-radius, rounded edge was oriented parallel to the sliding direction. Therefore, the sharp edges of the wedge's rake face played a major role in cutting the metal. The principal mechanism of metal removal was cutting action and subsequent chip formation in front of the wedge's rake face (Fig. 5.6). The coefficient of friction and the volume of metal displaced linearly decreased as the Vickers hardness increased at slopes of –0.77 and –1.61, respectively,

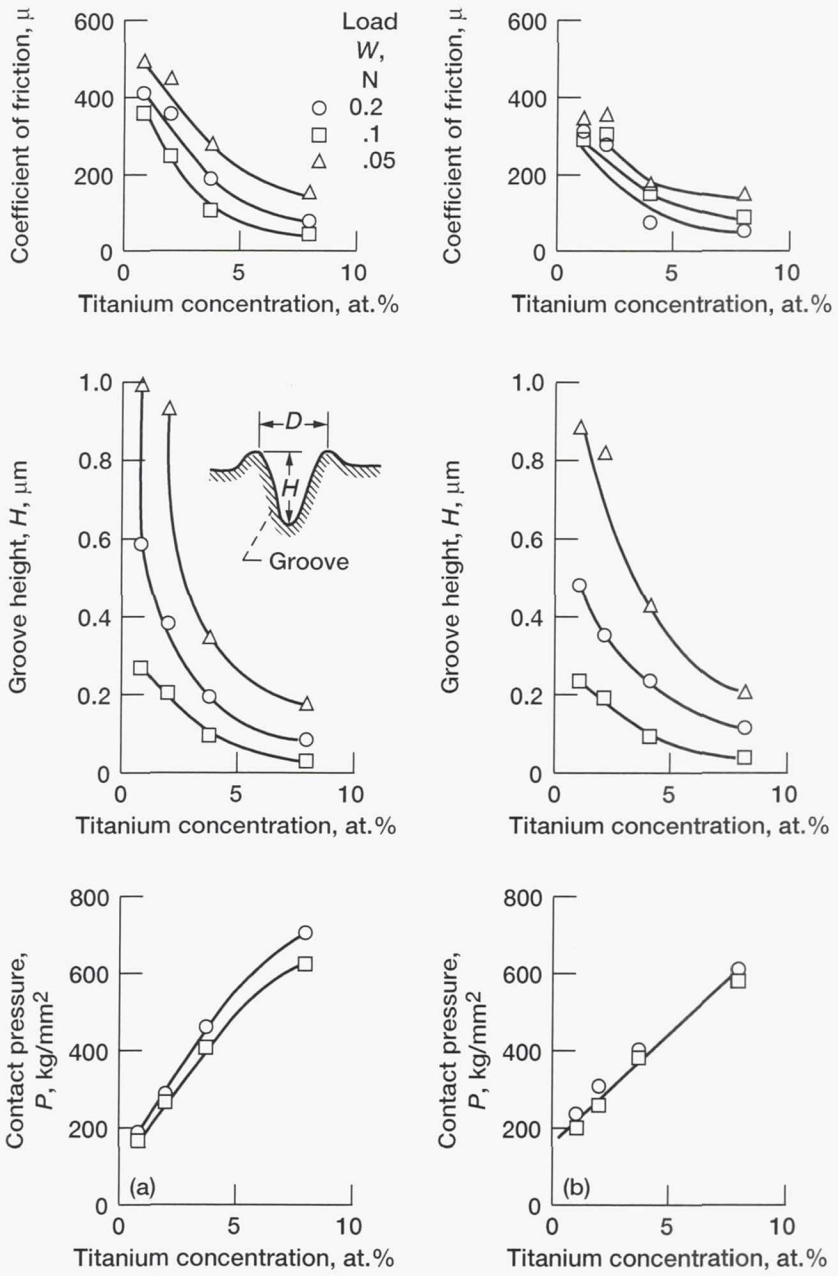

Figure 5.19.—Coefficient of friction, groove height, and contact pressure (calculated) as function of titanium concentration for annealed and mechanically polished Fe-Ti alloys. Same conditions as for Fig. 5.15. (a) Annealed surface. (b) Polished surface.

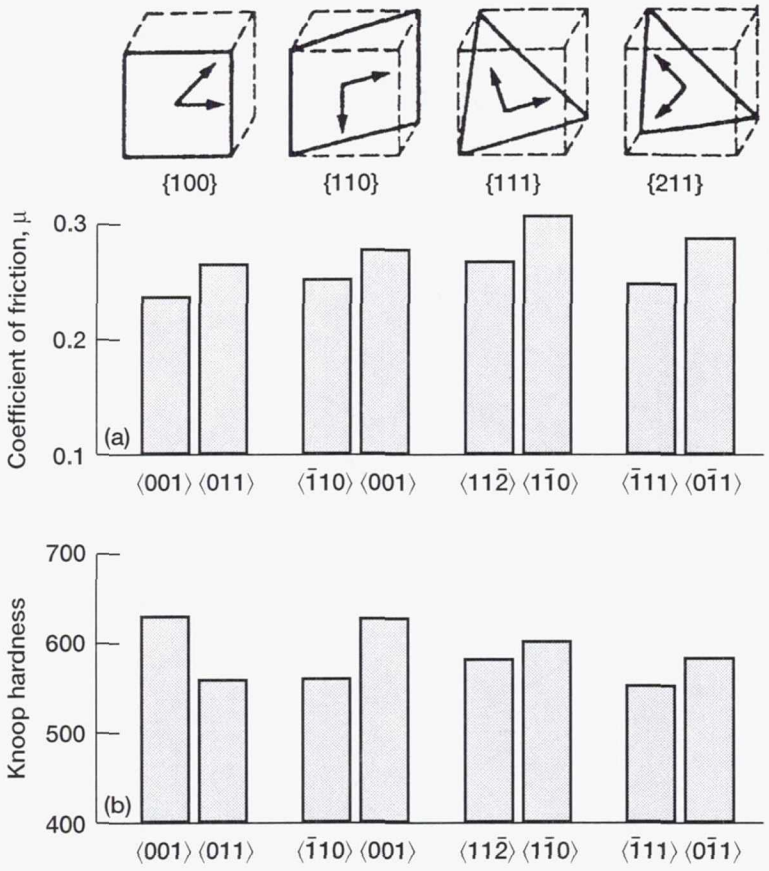

Figure 5.20.—Anisotropies on {100}, {110}, {111}, and {211} surfaces of Mn-Zn ferrite in laboratory air at room temperature. (a) Coefficient of friction; single-pass sliding of diamond pin (20-μm radius); sliding velocity, 3 mm/min; load, 1 N. (b) Knoop hardness; load, 3 N.

on logarithmic coordinates. The metal's wear resistance linearly increased as the Vickers hardness increased at a slope of 1.61 on logarithmic coordinates.

Figure 5.22 presents comparative data using a 50-μm-radius, spherical diamond pin (Fig. 5.4(a)). Again, all the variables correlated with the Vickers hardness. The coefficient of friction and the volume of metal displaced linearly decreased as the Vickers hardness increased at slopes of –0.35 and –1.33, respectively, on logarithmic coordinates. The metal's wear resistance linearly increased as the Vickers hardness increased at a slope of 1.33 on logarithmic coordinates.

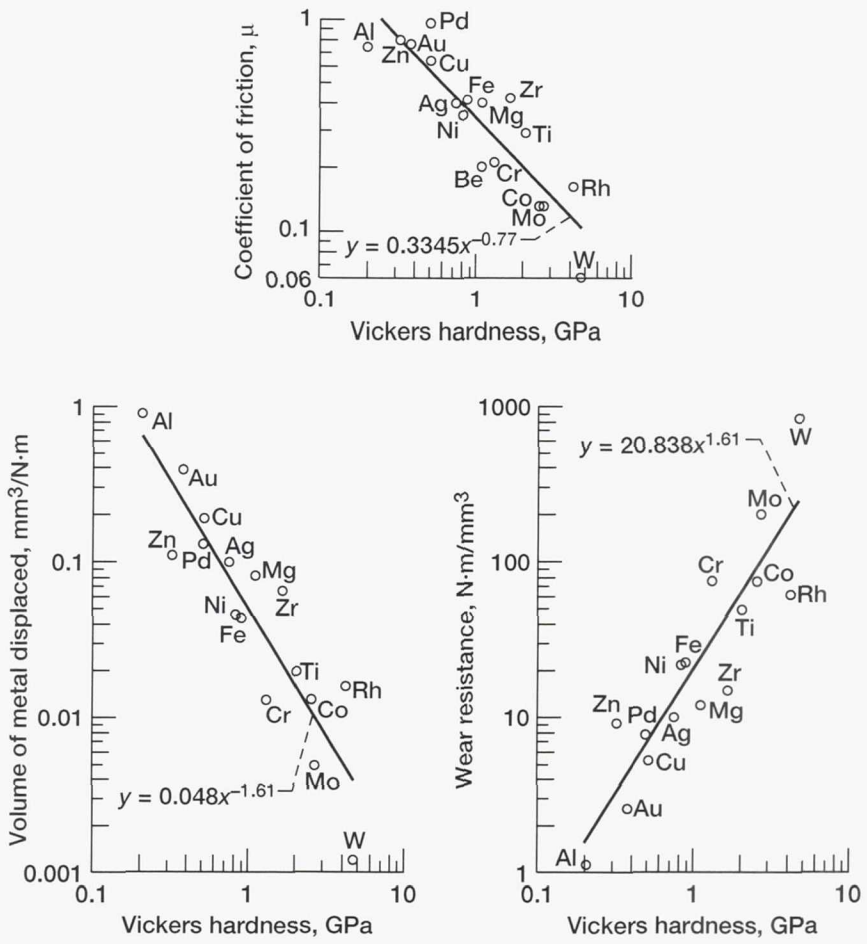

Figure 5.21.—Coefficient of friction, volume of metal displaced in unit load and unit distance, and wear resistance as function of Vickers hardness for various metals as a result of single-pass sliding of diamond wedge pin. Load, 0.2 N.

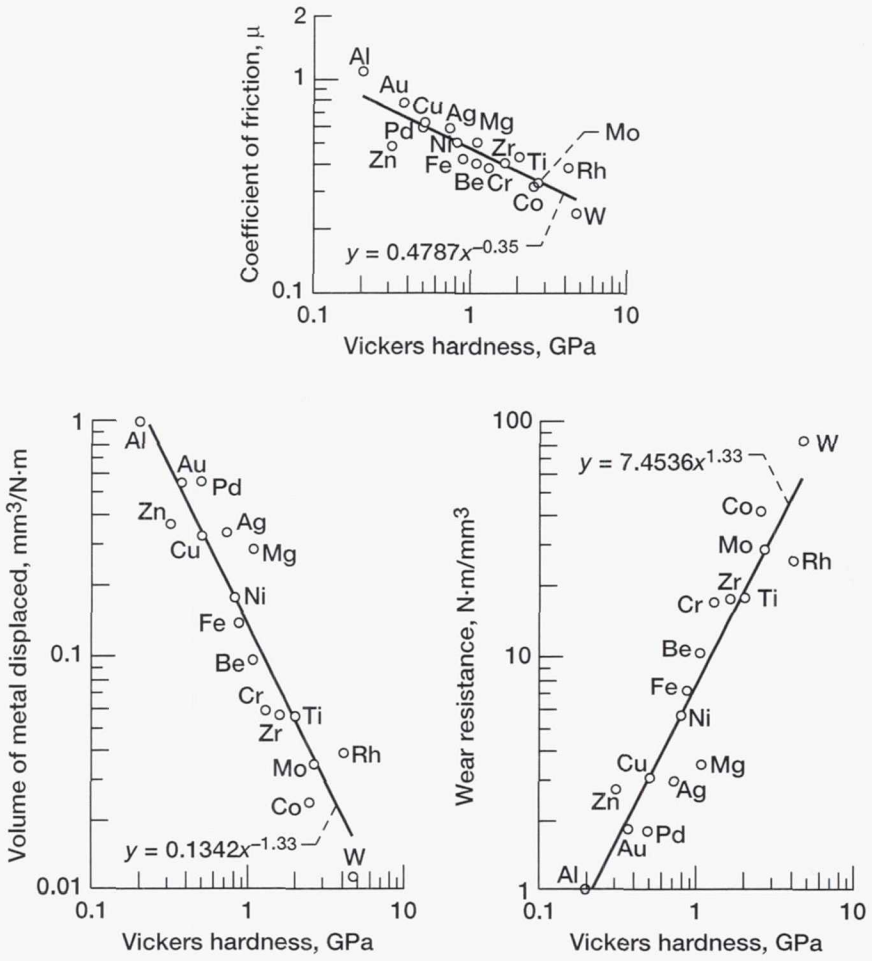

Figure 5.22.—Coefficient of friction, volume of metal displaced in unit load and unit distance, and wear resistance as function of Vickers hardness for various metals as a result of single-pass sliding of 50-μm-radius, spherical diamond pin. Load, 1 N.

5.4 Two- and Three-Body Abrasion by Hard Particles

When a number of grits of hard abrasive material (e.g., SiC and Al_2O_3) embedded in a resin matrix (binder) come into contact with a softer material (the two-body condition), the abrasive grits begin to cut or skive grooves in the softer material surfaces [5.36]. Abrasive wear can also occur when a third particle harder than one or both of the surfaces in contact becomes trapped at the interface. It can then remove material from one or both surfaces. This mode of wear is called three-body abrasion [5.36].

Many investigators have found that the abrasive wear of metals increases as the grit size increases up to a critical value and, thereafter, is independent of grit size [5.36]. The critical grit diameter is in the range 30 to 150 μm but strongly depends on abrasives, materials, and conditions, such as load, velocity, and environment. The grit size effect has also been found to hold for ceramic materials [5.37, 5.38]. For example, as shown in Fig. 5.23 the specific wear rate of polycrystalline Mn-Zn ferrite strongly depended on grit size in both two- and three-body abrasion, decreasing rapidly as grit size decreased. Detailed information on these results is provided in the following sections.

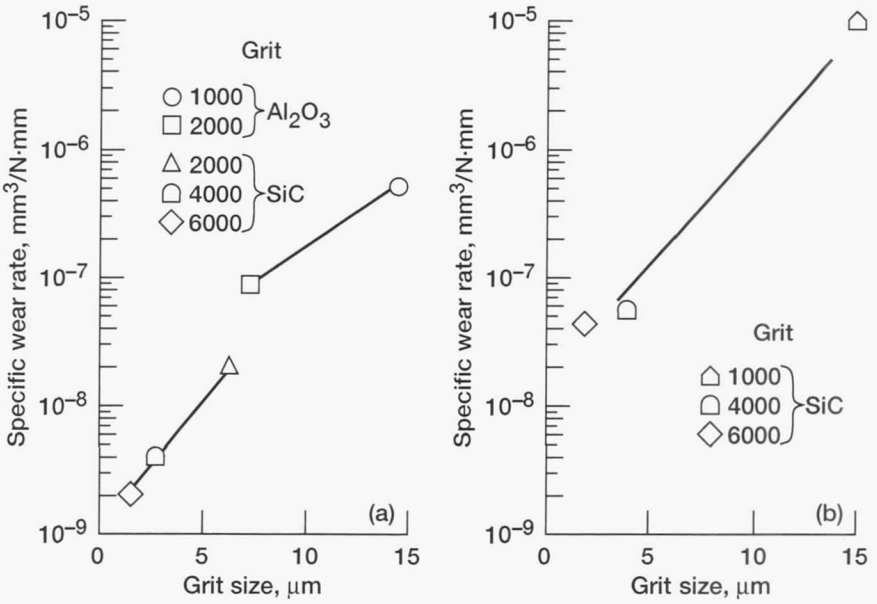

Figure 5.23.—Specific wear rate as function of grit size for polycrystalline Mn-Zn ferrite. (a) Two-body conditions. Abrasive-impregnated tapes; sliding velocity, 0.52 m/s; laboratory air; room temperature. (b) Three-body conditions. Lapping disk, cast iron; lapping fluid, olive oil; sliding velocity, 0.5 m/s; abrasive/fluid ratio, 27 wt.%; apparent contact pressure, 4 N/cm^2.

5.4.1 Two-Body Abrasion

The two-body abrasion study (Fig. 5.24(a), [5.37]) used abrasive-impregnated tapes, commonly called lapping tapes. The lapping tapes consisted of SiC or Al_2O_3 powder of various grit sizes in a polymeric binder on polyester films. The abrasive layer resembled emery paper, a familiar abrasive. The lapping tape sliding on an Mn-Zn ferrite generated abrasion (as shown in Chapter 2, Figs. 2.11 and 2.13). The ferrite wear surface revealed many plastically deformed grooves in the sliding direction formed primarily by the plowing action of abrasive particles in the lapping tape. The groove width increased as the grit size increased. Again, the wear rates of the polycrystalline Mn-Zn ferrite shown in Fig. 5.23(a) strongly depended on the kind of abrasive grit and its size. The wear rate for grits of the same kind increased rapidly as grit size increased. However, the coefficient of friction depended only on the kind of abrasive grit and was independent of grit size. The coefficient of friction was approximately 0.4 with Al_2O_3-grit lapping tapes but only 0.2 with SiC-grit lapping tapes.

Another interesting point to be observed from Fig. 5.23(a) is that, in spite of the nearly same grit size of 7.1 μm for Al_2O_3 and 6.3 μm for SiC, Al_2O_3 was approximately five times more abrasive than SiC. This difference may be related to the property, shape, and size distribution of abrasive particles on the tape as well as the degree to which the particles were enclosed by the binder.

Figure 5.24 presents the deformed-layer thickness for the Mn-Zn ferrite {110} plane sliding against lapping tapes as a function of grit size (see also Section 2.2.2). The deformed-layer thickness, as determined with reflection electron diffraction by depth profiling, increased as the grit size increased [5.39]. With 2.7-μm-SiC-grit lapping tape the deformed layer was 0.5 to 0.6 μm thick; with 14-μm-Al_2O_3-grit lapping tape the deformed layer was 0.8 to 0.9 μm thick. The deformed-layer

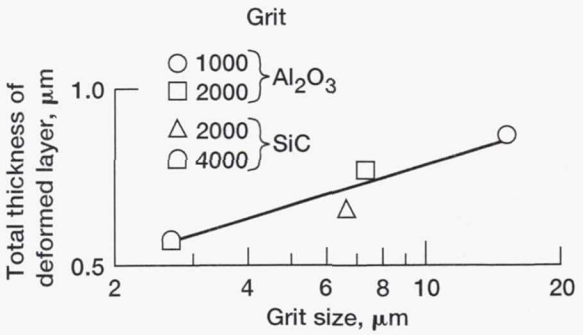

Figure 5.24.—Total thickness of deformed layer as function of grit size for Mn-Zn ferrite {110} plane in single-pass sliding contact with various lapping tapes. Initial tape tension, 0.3 N; head displacement, 120 ± 5 μm.

thickness, as determined with chemical-etching-rate depth profiling, also increased as the grit size increased.

Figure 5.25 presents the wear volume for four crystallographic planes of single-crystal Mn-Zn ferrite, {100}, {110}, {111}, and {211}, sliding against a grit-impregnated lapping tape as a function of the Vickers hardness of the wear surfaces [5.39]. Wear volume was influenced by crystallographic orientation, {110} < {100} < {111} < {211}, and by Vickers hardness. The slip (most closely packed) planes of Mn-Zn ferrite {110} exhibited the highest resistance to the two-body abrasion. Wear volume was inversely proportional to the Vickers hardness of the abraded ferrite wear surface. It, therefore, appears that the relationship of wear volume to Vickers hardness is similar for ceramics and metals.

5.4.2 Three-Body Abrasion

The three-body abrasion study (Fig. 5.23(b)) used a polishing machine capable of measuring friction during three-body abrasion. The apparatus (Fig. 5.26) contains a 160-mm-diameter, gray cast iron disk (lapping plate), a gray cast iron

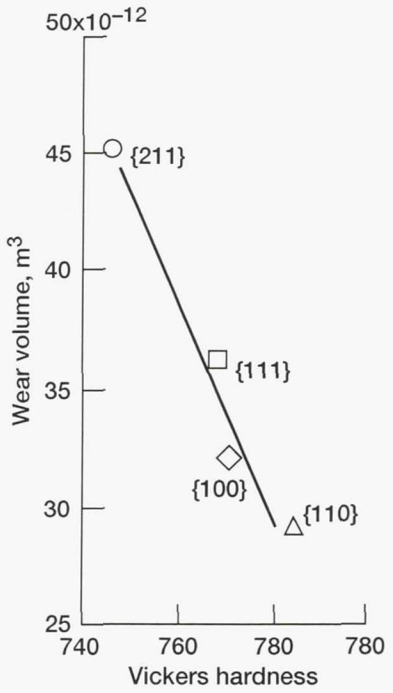

Figure 5.25.—Anisotropy of wear as function of Vickers hardness for {100}, {110}, {111}, and {211} planes of Mn-Zn ferrite. Sliding direction, ⟨110⟩; lapping tape, 2000-grit Al_2O_3; sliding velocity, 11 m/s; laboratory air; room temperature; measuring load, 0.25 N.

conditioning ring (72-mm outer diameter; 44-mm inner diameter), and an arm. The abrasive grits used (1000-, 4000-, and 6000-mesh SiC) have a cubelike shape with many sharp edges (Fig. 5.27). The grit shape does not depend on the grit size.

Figure 5.28 presents the grit size distribution of the SiC abrasives used in the study (i.e., the relative amounts of the various grits sizes in the powders). Because the grits were irregularly shaped, two dimensions (the largest diameter and the smallest diameter of each particle) were measured from the transmission electron micrographs. The bell-shaped curves reveal a generally strong correlation with the normal distribution. Therefore, they are expressed in terms of the normal density function. The average grit diameters and standard deviations are listed in Table 5.3. The 1000-, 4000-, and 6000-mesh SiC grits had average diameters of 15, 4, and 2 μm (with narrow tolerances), respectively. The crystalline shape of the SiC grits, particularly the shape along their largest diameter, makes them very sharp. Figure 5.29 presents the angle distribution of cutting edges of the abrasive grits along their largest diameter. The angle distributions were nearly the same for the 1000-, 4000-, and 6000-mesh SiC grits. Many edges had angles ranging from 90° to 100°.

The SiC grits abraded the single-crystal Mn-Zn ferrite surfaces in sliding contact under the three-body condition (as shown in Chapter 2, Fig. 2.12). The Mn-Zn ferrite wear was linearly proportional to the sliding distance, regardless of grit size,

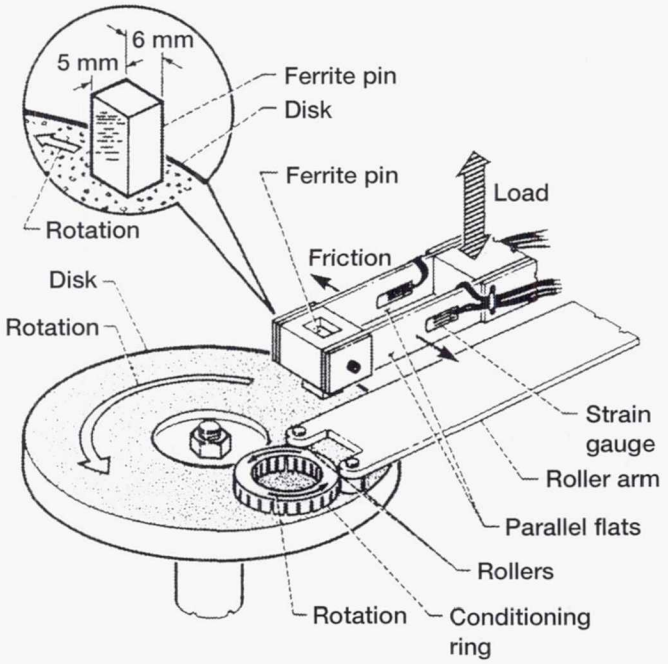

Figure 5.26.—Apparatus for three-body abrasive wear.

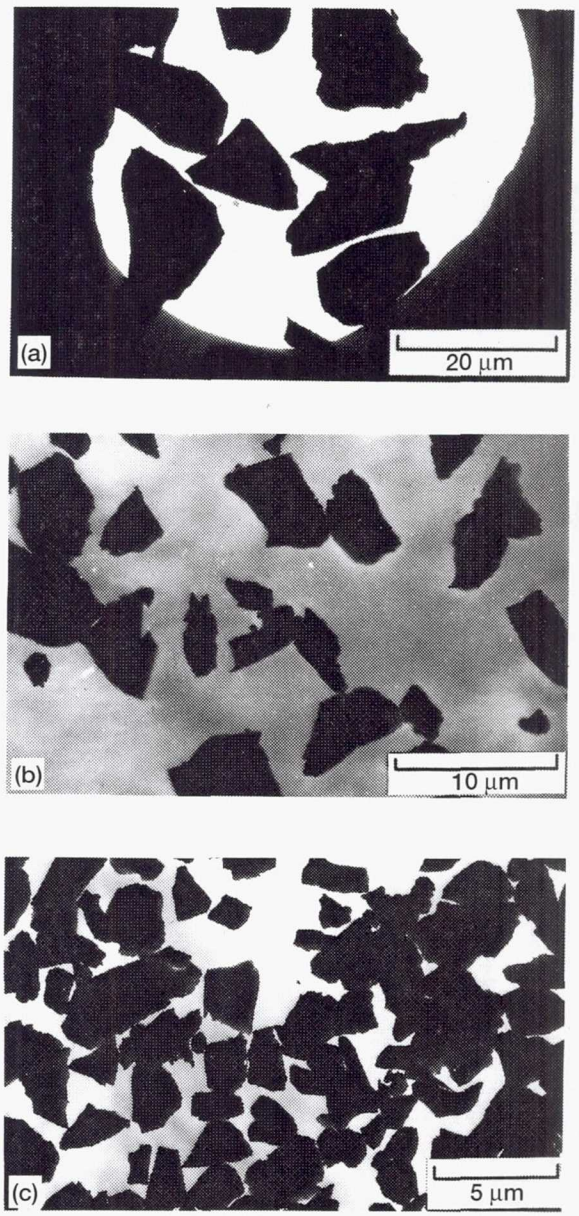

Figure 5.27.—Transmission electron micrographs of SiC abrasive grits. (a) 1000-mesh SiC. (b) 4000-mesh SiC. (c) 6000-mesh SiC.

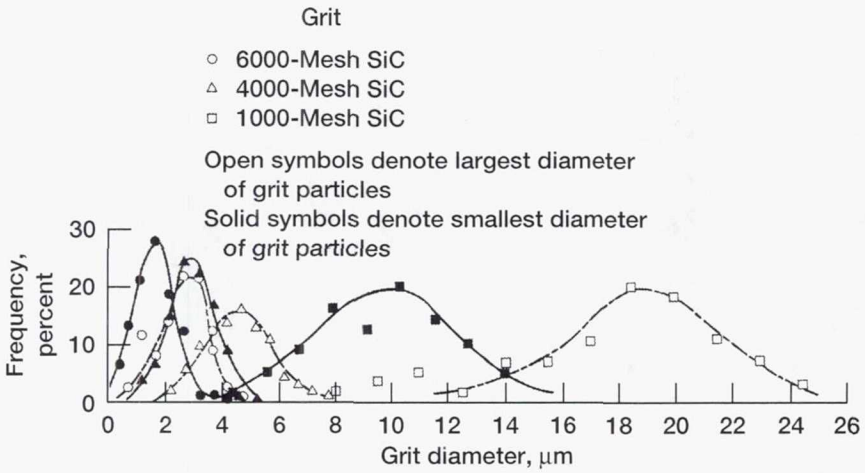

Figure 5.28.—Grit size distribution of 1000-, 4000-, and 6000-mesh SiC abrasives.

TABLE 5.3.—ABRASIVE GRIT SIZE IN THREE-BODY ABRASION STUDY

	1000-Mesh SiC	4000-Mesh SiC	6000-Mesh SiC
Average of smallest diameters of grit particles, μm	11.2	3.0	1.8
Average of largest diameters of grit particles, μm	17.9	4.5	2.7
Average grit diameter, μm	14.6	3.8	2.3
Ratio of largest to smallest grit diameter	1.7	1.6	1.7
Standard deviation of smallest grit diameters, μm	0.4	0.4	0.4
Standard deviation of largest grit diameters, μm	0.6	0.7	0.5
Standard deviation of average grit diameters, μm	0.4	0.5	0.3
Standard deviation of ratio of largest to smallest grit diameters	0.1	0.1	0.1

and was highly reproducible. However, the abrasion mechanism changed drastically with grit size. With 15-μm (1000-mesh) SiC grits, ferrite abrasion was caused principally by brittle fracture (Fig. 2.12(a)); but with the 4- and 2-μm (4000- and 6000-mesh) SiC grits, abrasion was caused by plastic deformation and fracture (Fig. 2.12(b)). Considerable microcracking (with 15-μm SiC grits) or plastic flow and fracture (with 4- and 2-μm SiC grits) drastically changed the crystalline state of the single-crystal ferrite surfaces to polycrystalline.

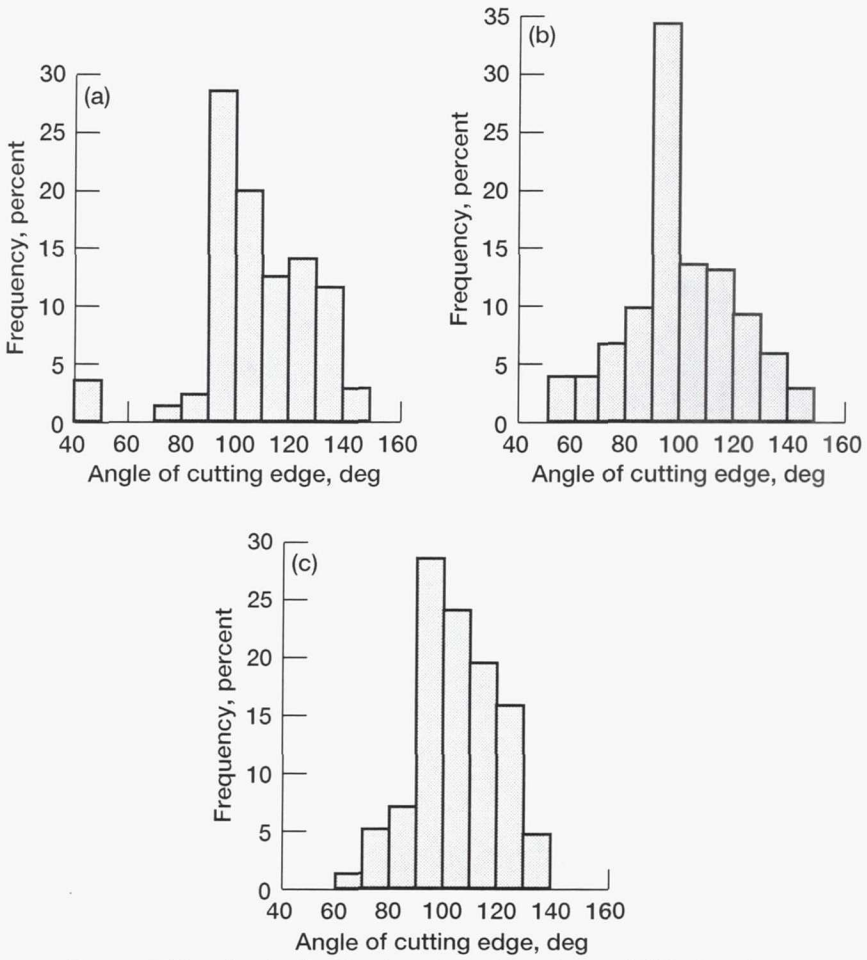

Figure 5.29.—Angle distribution of cutting edges of SiC abrasives. (a) 1000-mesh SiC. (b) 4000-mesh SiC. (c) 6000-mesh SiC.

The specific wear rate, wear surface roughness, and total deformed-layer thickness strongly depended on grit size. The specific wear rate (Fig. 5.23(b)) increased rapidly as grit size increased. The wear surface roughness (R_{max}, maximum height of irregularities) for single-crystal {100} Mn-Zn ferrites abraded in the ⟨110⟩ direction increased as grit size increased (not shown). It was 10 to 15 times greater (R_{max} = 2.2 μm) when abraded by 15-μm SiC grits than when abraded by 4- and 2-μm SiC grits (R_{max} = 0.21 and 0.17 μm, respectively). Figure 5.30 presents schematic structures for the deformed layers of the abraded single-crystal {100} Mn-Zn ferrites as a function of etching depth (depth from the wear surface). The total deformed-layer thickness, as determined with reflection electron diffraction

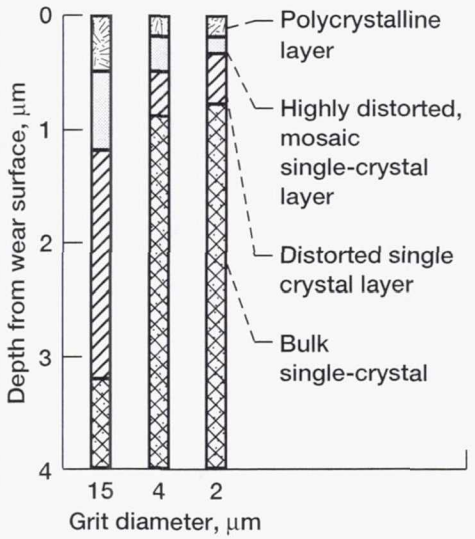

Figure 5.30.—Deformed layer produced on single-crystal {100} surface of Mn-Zn ferrite as function of grit size under three-body abrasion. Apparent contact pressure, 4 N/cm^2; sliding direction, $\langle 0\bar{1}1 \rangle$.

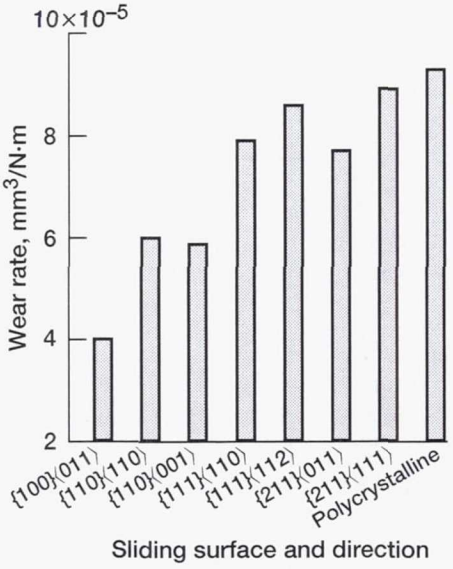

Figure 5.31.—Anisotropies on {100}, {110}, {111}, and {211} surfaces of Mn-Zn ferrite for 15-μm SiC grits under three-body abrasion.

by depth profiling, increased markedly as grit size increased. The deformed layers were 3 μm for the ferrite abraded by 15-μm SiC, 0.9 μm for the ferrite abraded by 4-μm SiC, and 0.8 μm for the ferrite abraded by 2-μm SiC.

Figure 5.31 presents specific wear rates under three-body conditions for four crystallographic planes of single-crystal Mn-Zn ferrite, {100}, {110}, {111}, and {211}, abraded with 15-μm SiC grits in different directions and for a polycrystalline Mn-Zn ferrite also abraded with 15-μm SiC grits. The wear rates of the single-crystal ferrite surfaces varied with crystallographic plane and direction. The polycrystalline ferrite exhibited the weakest wear resistance to abrasion because of grain boundary weakness.

References

5.1 *Glossary of Terms and Definitions in the Field of Friction, Wear, and Lubrication*, Research Group on Wear of Engineering Materials, Organization for Economic Cooperation and Development (OECD), Paris, 1969.

5.2 P.A. Engel, *Impact Wear of Materials*, Vol. 2, Elsevier Scientific Publishing Co., Amsterdam, 1978.

5.3 H. Czichos, *Tribology—A Systems Approach to the Science and Technology of Friction, Lubrication, and Wear*, Vol. 1, Elsevier Scientific Publishing Co., New York, 1978.

5.4 T.S. Eyre, Wear characteristics of metals, *Trib. Int. 9, 5*: 203–212 (1976).

5.5 M.M. Krushchov and M.A. Babichev, Resistance to abrasive wear and elasticity modulus of metals and alloys, *Soviet Physics-Doklady 5*: 410–412 (1960–61).

5.6 B.W.E. Avient, J. Goddard, and H. Wilman, An experimental study of friction and wear during abrasion of metals, *Proc. R. Soc. London A 258, 1293*: 159–180 (1960).

5.7 E. Rabinowicz, L.A. Dunn, and P.G. Russell, A study of abrasive wear under three-body conditions, *Wear 4*: 345–355 (1961).

5.8 S.I. Hayashi, Hydrogen introduction by abrasion in aluminum, *Japanese J. Appl. Phys. 35, 12A*: 6191–6199 (1996).

5.9 R.A.H. Edwards and W. Eichenauer, Reversible hydrogen trapping at grain-boundaries in superpure aluminum, *Scr. Metall. 14, 9*: 971–973 (1980).

5.10 K. Miyoshi and D.H. Buckley, Occurrence of spherical ceramic debris in indentation and sliding contact, NASA TP–2048 (1982).

5.11 K. Miyoshi and D.H. Buckley, The friction and wear of metals and binary alloys in contact with an abrasive grit of single-crystal silicon carbide, *ASLE Trans. 23, 4*: 460–472 (1980).

5.12 R.P. Steijn, On the wear of sapphire, *J. Appl. Phys. 32, 10*: 1951–1958 (1961).

5.13 R.P. Steijn, Sliding and wear in ionic crystals, *J. Appl. Phys. 34, 2*: 419–428 (1963).

5.14 R.P. Steijn, Friction and wear of single crystals, *Wear 7*: 48–66 (1964).

5.15 R.P. Steijn, Friction and wear of rutile single crystals, *ASLE Trans. 12, 1*: 21–33 (1969).

5.16 K.F. DuFrane and W.A. Glaeser, Study of rolling-contact phenomena in magnesium oxide, NASA CR–72295 (1967).

5.17 K. Miyoshi and D.H. Buckley, Friction, deformation, and fracture of single-crystal silicon carbide, *ASLE Trans. 22, 1*: 79–90 (1979).

5.18 K. Miyoshi, D.H. Buckley, S.A. Alterovitz, J.J. Pouch, and D.C. Liu, Adhesion, friction, and deformation of ion-beam-deposited boron-nitride films, *International Conference on Tribology—Friction, Lubrication, and Wear: Fifty Years On*, Vol. 11, Mechanical Engineering Publications, London, 1987, pp. 621–628.

5.19 K. Miyoshi, D.H. Buckley, J.J. Pouch, S.A. Alterovitz, and H.E. Sliney, Mechanical strength and tribological behavior of ion-beam-deposited BN films on nonmetallic substrates, *Surf. Coat. Technol. 33*: 221–233 (1987). (Also NASA TM–89818.)

5.20 F.P. Bowden and D. Tabor, *The Friction and Lubrication of Solids*, Part II, Clarendon Press, Oxford, UK, 1964, pp. 158–185.

5.21 K. Miyoshi and D.H. Buckley, Anisotropic tribological properties of SiC, *Wear 75, 2:* 253–268 (1982).

5.22 D.H. Buckley and K. Miyoshi, Friction and wear of ceramics, *Wear 100, 1–3*: 333–353 (1984).

5.23 K. Miyoshi, D.H. Buckley, and B. Bhushan, Friction and morphology of magnetic tapes in sliding contact with nickel-zinc ferrite, NASA TP–2267 (1984).

5.24 K. Miyoshi, Adhesion, friction, and micromechanical properties of ceramics, *Surf. Coat. Technol. 36, 12*: 487–501 (1988).

5.25 D. Tabor, *The Hardness of Metals*, Clarendon Press, Oxford, UK, 1951, pp. 6–18.

5.26 M.F. Stroud and H. Wilman, The proportion of the groove volume removed as wear in abrasion of metals, *Brit J. Appl. Phys. 13*: 173–178 (1962).

5.27 T.O. Mulhearn and L.E. Samuels, The abrasion of metals: a model of the process, *Wear 5*: 478–498 (1962).

5.28 J. Larsen-Basse, Influence of grit size on the groove formation during sliding abrasion, *Wear 11*: 213–222 (1968).

5.29 I.V. Kragelskii, *Friction and Wear*, Butterworths, Washington, 1965, pp. 20–26, 88–110.

5.30 W.C. Leslie, Iron and its dilute substitutional solid solutions, *Metall. Trans. 3*: 5–26 (1972).

5.31 W.A. Spitzig and W.C. Leslie, Solid-solution softening and thermally activated flow in alloys of Fe with three atomic % Co, Ni, or Si, *Acta Metall. 19, 11*: 1143–1152 (1971).

5.32 E. Pink, Legierungsentfestigung in kubisch-raumzentrierten Metallen (Alloy softening in body-centered cubic metals), *Zeitschrift fuer Metallkunde 64, 12*: 871–881 (1973).

5.33 D. Leemans and M.E. Fine, Solid solution softening and strain-rate sensitivity of Fe-Re and Fe-Mo alloys, *Metall. Trans. 5, 6*: 1331–1336 (1974).

5.34 J.R. Stephens and W.R. Witzke, Alloy softening in binary iron solid solutions, *J. Less-Common Metals 48, 2*: 285–308 (1976).

5.35 K. Miyoshi and D.H. Buckley, Friction and wear with a single-crystal abrasive grit of silicon carbide in contact with iron-base binary alloys in oil—effects of alloying element and its content, NASA TP–1394 (1979).

5.36 E. Rabinowicz, *Friction and Wear of Materials*, John Wiley & Sons, New York, 1964.

5.37 K. Miyoshi, Lapping of manganese-zinc ferrite by abrasive tape, *Lubr. Eng., 38, 3*: 165–172 (1982).

5.38 K. Miyoshi, Effect of abrasive grit size on wear of manganese-zinc ferrite under three-body abrasion, *Tribology and Mechanics of Magnetic Storage Systems* (B. Bhushan and N.S. Eiss, Jr., eds.), STLE SP–22, Vol. IV, 1987, pp. 123–132.

5.39 K. Miyoshi, D.H. Buckley, and K. Tanaka, Effect of crystallographical and geometrical changes of a ferrite head on magnetic signals during the sliding process with magnetic tape, *Tribology and Mechanics of Magnetic Storage Systems*, ASLE SP–21, Vol III, 1986, pp. 42–49.

5.40 K.A. Gschneider, Jr., Physical properties and interrelationships of metallic and semimetallic elements, *Solid State Physics*, Chapt. 16, F. Seitz and D. Turnbull, eds., Academic Press, 1965, pp. 275–426.

5.41 C.S. Barrett, *Structure of Metals, Crystallographic Methods, Principles, and Data*, McGraw-Hill, New York, 1943, pp. 552–554.

REPORT DOCUMENTATION PAGE

Form Approved
OMB No. 0704-0188

1. AGENCY USE ONLY (*Leave blank*)	2. REPORT DATE	3. REPORT TYPE AND DATES COVERED
	August 2001	Technical Memorandum

4. TITLE AND SUBTITLE

Solid Lubrication Fundamentals and Applications
Abrasion: Plowing and Cutting

5. FUNDING NUMBERS

WU–505–63–5A

6. AUTHOR(S)

Kazuhisa Miyoshi

7. PERFORMING ORGANIZATION NAME(S) AND ADDRESS(ES)

National Aeronautics and Space Administration
John H. Glenn Research Center at Lewis Field
Cleveland, Ohio 44135–3191

8. PERFORMING ORGANIZATION REPORT NUMBER

E–9863-5

9. SPONSORING/MONITORING AGENCY NAME(S) AND ADDRESS(ES)

National Aeronautics and Space Administration
Washington, DC 20546–0001

10. SPONSORING/MONITORING AGENCY REPORT NUMBER

NASA TM—2001-210749/
Chapter 5

11. SUPPLEMENTARY NOTES

Responsible person, Kazuhisa Miyoshi, organization code 5140, 216–433–6078.

12a. DISTRIBUTION/AVAILABILITY STATEMENT

Unclassified - Unlimited
Subject Category: 27 Distribution: Nonstandard
Available electronically at http://gltrs.grc.nasa.gov/GLTRS
This publication is available from the NASA Center for AeroSpace Information, 301–621–0390.

12b. DISTRIBUTION CODE

13. ABSTRACT ***(Maximum 200 words)***

Chapter 5 presents abrasion, a common wear phenomenon of great economic importance. It has been estimated that 50% of the wear encountered in industry is due to abrasion. Also, it is the mechanism involved in the finishing of many surfaces. Experiments are described to help in understanding the complex abrasion process and in predicting friction and wear behavior in plowing and/or cutting. These experimental modelings and measurements used a single spherical pin (asperity) and a single wedge pin (asperity). Other two-body and three-body abrasion studies used hard abrasive particles.

14. SUBJECT TERMS

Solid lubrication; Coatings; Tribology fundamentals; Applications

15. NUMBER OF PAGES

42

16. PRICE CODE

17. SECURITY CLASSIFICATION OF REPORT	18. SECURITY CLASSIFICATION OF THIS PAGE	19. SECURITY CLASSIFICATION OF ABSTRACT	20. LIMITATION OF ABSTRACT
Unclassified	Unclassified	Unclassified	